AD-A125 278 SENSITIVITY TO SOUND SPEED OF SURFACE/BOTTOM REFLECTING TRANSMISSIONS IN A.. (U) RENSSELAER POLYTECHNIC INST TROY NY DEPT OF MATHEMATICAL SCIE.. 1/1

UNCLASSIFIED W L SIEGMANN ET AL. 01 FEB 83 RPI-MATH-136. F/G 20/1 NL

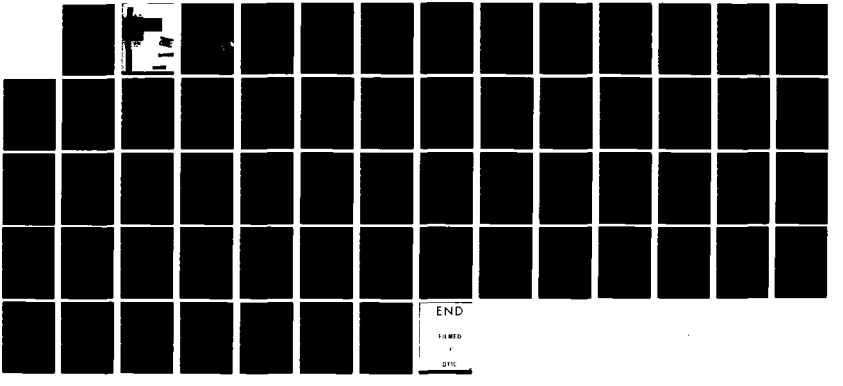

END

FILMED

DTIC

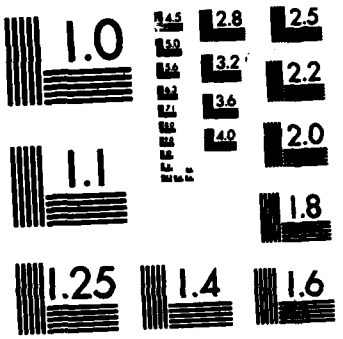

MICROCOPY RESOLUTION TEST CHART
NATIONAL BUREAU OF STANDARDS-1963-A

AD A125278

Sensitivity to sound speed of surface/ bottom reflecting transmissions in a deep ocean channel

by

W. L. Siegmann, M. J. Jacobson
and P. Bilazarian

DTIC
ELECTE
MAR 7 1983
H

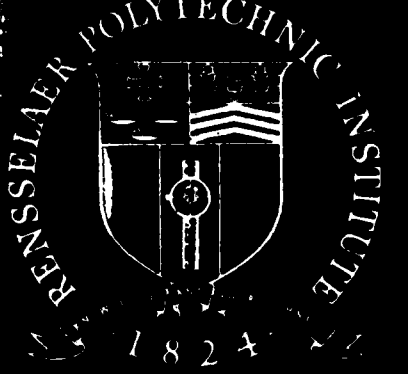

DISTRIBUTION STATEMENT A
Approved for public release;
Distribution Unlimited

Rensselaer Polytechnic Institute
Troy, New York 12181

DTIC FILE COPY

83 03 04 039

83 03 04 039

Sensitivity to sound speed of surface/ bottom reflecting transmissions in a deep ocean channel

by

W. L. Siegmann, M. J. Jacobson
and P. Bilazarian

Department of Mathematical Sciences

Rensselaer Polytechnic Institute

Troy, New York 12181

DTIC
ELECTE
MAR 7 1983
H

RPI Math. Rep. No. 136

February 1, 1983

This work was sponsored by
Code 425, Office of Naval Research
Contract No. N00014-76-C-0288
NR 386-606

This document has been approved for public release and sale; its distribution is unlimited.

ABSTRACT

The sensitivity of oceanic sound transmissions to the choice of a sound-speed profile is analyzed using ray theory. The profile may be selected from a large depth-dependent collection which models the deep ocean sound channel. Sound propagation is examined between fixed source and receiver, both close to horizontal ocean boundaries, for ranges up to about 50 km. Given a specified profile, procedures are prescribed for constructing a second, simpler profile so that important acoustic quantities are virtually identical. The construction methods are easy to apply, have physical interpretations, and identify the critical aspects of profile data which influence transmissions. The ray geometries associated with the two profiles are shown to be very close. Useful formulas are derived which demonstrate that per-ray and total-field phases and amplitudes corresponding to the simpler profile approximate accurately those of the specified profile. Schemes are presented for determining range intervals for replacement of the given profile, based on specified tolerances for phase and amplitude differences. Thus, when our procedure is applied, propagation results are not sensitive to the type of profile selected.

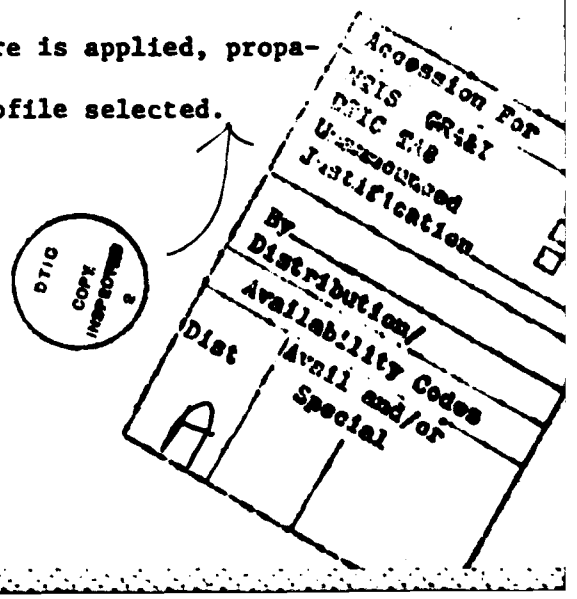

INTRODUCTION

The investigation of any oceanic sound transmission problem requires the prior specification of a sound-speed structure in some way, such as by fitting data. We address an important sensitivity issue which has received little or no attention previously. We seek methods to replace a specified sound-speed profile by a simpler type of profile so that significant acoustic quantities with the two profiles are negligibly different. Previous sensitivity studies have noted differences that can be caused by sound-speed variations. For instance, an investigation[1] of the sensitivity of ray theory to small changes in environmental data documents large changes in transmission loss at ranges less than 20 km resulting from small, randomly perturbed variations in a linear profile. For another example, one portion of a study[2] concerned with propagation loss in shallow water displays large variations in normal-mode transmission loss at ranges from 10 km to 100 km, that are associated with a family of decreasing profiles having the same average gradient. In addition, there has been much published concerning the relative advantages of one type of sound-speed profile over others, as for instance in Refs. 3-7. Indeed, one trend among such studies has been different from our aim, in the sense of advocating for various reasons the replacement of one type of sound-speed profile by a more complicated type. For example, the discovery[3] of possible inaccuracies in acoustic intensity for special transmission situations caused by slope discontinuities in piecewise-linear sound-speed profiles supported the use of more elaborate profiles with curved segments. Our motivation is not inconsistent with such results, but is, rather, to specify situations and find methods for the replacement of given profiles by simpler ones.

There are several important advantages of effecting the replacement

of a given profile by an acoustically equivalent, simpler one. First, formulas for significant acoustic quantities may be made more convenient, useful, and easily interpreted. Second, the simpler profile, along with the concomitant procedure for its construction, identifies the critical aspects of profile data which influence transmission results. For example, with the profile types and particular transmission problems considered here, the depth average of the profile data as well as data near particular ocean depths turn out to be critical. Therefore, it is these features of the data, rather than the individual data points themselves, that must be modeled by the sound-speed profile in a transmission problem. A third advantage is connected to the fact that, in many propagation studies which analyze the influence of complicated environmental phenomena on sound transmissions, it is essential to make various simplifying assumptions. Typically, these include modeling the sound-speed distribution for the ocean region of interest with a relatively simple type of profile. For example, bilinear approximations to sound-speed structures have been used to analyze short-range acoustic transmission in cyclonic eddies[8] and long-range SOFAR transmission fluctuations produced by a Rossby wave.[9] Thus, sound-speed profile replacement results of the type in this paper offer an obvious means for extending conclusions and predictions of propagation studies, which assume a relatively simple profile, to situations with more complicated and realistic profiles.

We consider here a fairly general class of depth-dependent sound-speed profiles which characterize the deep-ocean sound channel. This channel has been long recognized as a principal feature of the sound-speed distribution in many regions of the abyssal oceans. The issue of profile-

replacement sensitivity becomes of special and practical significance for the sound channel, in view of the rich abundance of distinct profiles developed over the years to describe it. Some of these profiles, containing various parameters, are the bilinear,[10] multilinear,[11] hyperbolic-linear,[12] parabolic,[13] squared index of refraction quadratic,[14] Eckart,[15] and those contained in Refs. 4-7. The collection of deep-ocean channel profiles we consider also includes those which can be constructed numerically by interpolation.[16]

We assume in this study that the ocean boundaries are horizontal. This assumption, along with that of no horizontal or temporal variation in sound-speed structure, comprise a fundamental model of sound transmission through a deep-ocean sound channel, from which more complicated models are developed by perturbations. Thus, positive profile-replacement sensitivity results for this situation can be anticipated to be germane to a variety of more complicated models. We employ ray theory and focus in this initial investigation on surface/bottom reflecting transmissions up to intermediate ranges between a source and receiver, each of which is located on or near either of the ocean boundaries. Our study can be extended to include a variety of source-receiver positions not on or near the ocean boundaries, different types of ray propagation, and larger transmission ranges. Such extensions, which involve both generalizations of our procedures here and new methods for constructing simpler replacement profiles, will be presented in future work.

We present one scheme in Sec. I for constructing from a specified sound-channel profile its simpler comparison profile of bilinear type. The ray geometries associated with these two profiles are shown to be very close. In Sec. II per-ray phases and amplitudes for the two profiles are demon-

strated to correspond closely, when the source-receiver range is not too large. Useful approximate formulas for per-ray phase and amplitude differences are developed to describe allowable ranges, for specified source frequency and acceptable phase-and-amplitude-difference tolerances. These per-ray results can be extended to longer transmission ranges, as described in Sec. III. A different method for choosing a bilinear comparison profile is presented there, in which the comparison profile is modified slightly at each longer range. In Sec. IV we compare received total fields associated with the specified sound-channel profile and its simpler comparison profile. Approximate formulas are presented for total-field phase and amplitude differences, which facilitate the determination of those ranges where the total fields match closely. Finally, major results are summarized in Sec. V.

I. SOUND-SPEED PROFILES AND RAY GEOMETRY

A. Sensitivity problem formulation

We first specify the types of sound-speed profiles to be considered in this investigation. These profiles $c(z)$ depend on depth z only, decreasing from the ocean surface at $z = 0$ to a minimum sound speed at positive depth $z = z_a$ and then increasing to the ocean bottom at $z = z_b$. The surface, SOFAR-axis, and bottom sound speeds of $c(z)$ are denoted by c_s, c_a, and c_b, respectively. On $0 \leq z \leq z_b$ we also require that $c(z)$ be continuous and piecewise continuously differentiable (i.e., possess a continuous derivative except possibly at a finite number of depths). We denote this collection of profiles by C. Since C is a quite general class, including profiles which are concave up, piece-wise concave down, or of

mixed concavity, it follows that typical depth-dependent, single-minimum profiles (for example, those described or used in Refs. 4-7 and 10-16) belong to C. We note that the procedures to be developed in this initial study could be extended to apply to other types of profiles.

The sound source S and receiver R, separated by a horizontal distance R, are taken for simplicity to be located on the ocean boundaries. We place the origin of our left-handed Cartesian coordinate system on the ocean surface either at or above S; the horizontal coordinate x is positive in the direction toward R, while the (depth) coordinate z is measured positive downward. We restrict this study to ranges which are less than that range R_c at which any of the rays is either tangent to one of the ocean boundaries or has a horizontal turning point. If S and R are both located on the ocean surface (or bottom), all rays for $R < R_c$ are either bottom reflected (BR) [or surface reflected (SR)] or surface-reflected/bottom-reflected (SRBR) types. If S and R are located on opposite boundaries, all rays are either direct (D) or SRBR types for $R < R_c$. The size of R_c depends on both the particular profile under consideration and the boundary locations of S and R. The basic procedures for constructing the simpler comparison profile from a given profile, and for determining those ranges less than R_c where important acoustic quantities associated with the two profiles correspond closely, are exactly the same for all such source-receiver locations. Furthermore, results display the same qualitative features. Therefore, we focus henceforth on the case where S and R are both located on the ocean surface, and we use the results for this case to obtain relevant conclusions for other cases.

As discussed in the Introduction, we formulate the sensitivity

analysis by singling out one simple profile type from C which is then used to compare with others in C. For this paper we choose to use a bilinear comparison profile, with sound speed decreasing linearly from $z = 0$ to its SOFAR-axis depth and then increasing linearly from this depth to $z = z_b$. From here on, any unbarred quantity will refer to a profile from the general class C, while any barred quantity will refer to a comparison bilinear profile. For any bilinear profile, there are four parameters required for its specification which, for example, could be taken as $\bar{z}_a$, $\bar{c}_s$, $\bar{c}_a$, and $\bar{c}_b$. The problem is to determine whether, and if so how, these parameters can be chosen so that corresponding acoustic quantities from a profile in C and from the comparison profile are negligibly different. We remark that one reason for using a bilinear comparison profile is that this profile type has been thoroughly analyzed.[10] Another reason is the simplicity of its ray geometry and of formulas for relevant acoustic quantities. We emphasize, however, that our approach is sufficiently general to permit straightforward extensions to the use of other types of comparison profiles.

B. Comparison profile: shorter ranges

We now present a method of constructing from a given $c(z) \in C$ a single bilinear comparison profile, labeled $\bar{c}_I(z)$, which may be used throughout an entire interval of shorter source-receiver ranges. This profile yields positive sensitivity results, in the sense that differences in corresponding acoustic quantities for the two profiles are insignificant. In Sec. III we shall present a second procedure for construction of comparsion profiles $\bar{c}_{II}(z)$ which provide positive sensitivity results over longer transmission ranges. A quantitative characterization of shorter and longer

ranges will be given subsequently.

For any specified profile $c(z) \in C$ and for all source-receiver boundary locations, the parameters of its unique, corresponding bilinear comparison profile $\bar{c}_I(z)$ are determined as follows:

(1) The depth-averaged sound speed of $\bar{c}_I(z)$ is set equal to that of $c(z)$;

(2) the SOFAR-axis depth $\bar{z}_a$, the surface sound speed $\bar{c}_s$, and the bottom sound speed $\bar{c}_b$ of $\bar{c}_I(z)$ are matched to those of $c(z)$.

The first condition is crucial in the construction of the $\bar{c}_I(z)$ profile, giving

$$\bar{c}_\mu \equiv z_b^{-1} \int_0^{z_b} \bar{c}_I(z)dz = z_b^{-1} \int_0^{z_b} c(z)dz \equiv c_\mu. \tag{1a}$$

As we shall show in Sec. II, equality of the average sound speeds c_μ and $\bar{c}_\mu$ serves to eliminate dominant terms in differences of per-ray acoustic quantities from $c(z)$ and $\bar{c}_I(z)$. From Eq. (1a) we obtain a simple equation relating the SOFAR-axis sound speed $\bar{c}_a$ and the three parameters mentioned in the second condition:

$$\bar{c}_a = [(\bar{c}_b - \bar{c}_s) z_b^{-1}] \bar{z}_a + 2c_\mu - \bar{c}_b. \tag{1b}$$

The surface and bottom sound speeds of $\bar{c}_I(z)$ are matched to those of $c(z)$ (i.e., $\bar{c}_s = c_s$ and $\bar{c}_b = c_b$) primarily for two reasons. First, these conditions are sufficient to guarantee that for any of the boundary locations of S and R, the ray types and numbers of received rays associated with $\bar{c}_I(z)$ and $c(z)$ are the same, for all ranges up to about R_c. Second, we shall see that these conditions assist in reducing per-ray amplitude differences. SOFAR-axis depths of $\bar{c}_I(z)$ and $c(z)$ are matched (i.e., $\bar{z}_a = z_a$) because we have determined that acoustic quantities in Sec. II are relatively

insensitive to the choice of $\bar{z}_a$. It follows from Eq. (1b) and the matchings of the second step that the four parameters of the bilinear profile $\bar{c}_I(z)$ are uniquely specified. Thus, we write

$$c_I(z) = \begin{cases} \bar{g}_u z + c_s & , \quad 0 \le z \le z_a \ , \\ \bar{g}_\ell (z-z_b) + c_b & , \quad z_a < z \le z_b \ , \end{cases} \tag{2a}$$

where

$$\bar{g}_u = (\bar{c}_a - c_s)/z_a \ , \quad \bar{g}_\ell = (c_b - \bar{c}_a)/(z_b - z_a) \ . \tag{2b}$$

The critical aspects of sound-speed profile data which are used to specify a c(z) profile in this situation are now apparent. The construction procedure for the $\bar{c}_I(z)$ profile implies that data near the surface, SOFAR axis and bottom are clearly important. Also, the role of the sound speed c_μ over the entire ocean depth identifies the data mean as critical.

We illustrate our procedures with a hyperbolic-linear sound-speed profile,[12] consisting of a combination of linear and hyperbolic-cosine functions and, for simplicity, select equal surface and bottom sound speeds. The solid curve in Fig. 1(a) is a graph of the $c^{(H)}(z)$ profile, given by

$$c^{(H)}(z) = \begin{cases} g_u z + c_s & , \quad 0 \le z \le z_u \ , \\ c_a \cosh[k_u (z-z_a)] & , \quad z_u < z \le z_a \ , \\ c_a \cosh[k_\ell (z-z_a)] & , \quad z_a < z \le z_\ell \ , \\ g_\ell (z-z_b) + c_s & , \quad z_\ell < z \le z_b \ . \end{cases} \tag{3a}$$

We use the same numerical values for z_u, z_a, z_ℓ, c_s, and c_a as in Ref. 17. Also, we compute the upper linear slope g_u, the parameter k_u, and the upper joining sound speed $c_u = c^{(H)}(z_u)$ by matching values and slopes of $c^{(H)}(z)$ at $z = z_u$, and similarly at $z = z_\ell$. Parameter values (to six significant digits) are

listed in the second column of Table I. If S and R are both located on the ocean surface or the ocean bottom, R_c is equal to 69.0 km for the $c^{(H)}(z)$ profile; if S and R are located on opposite boundaries, R_c is equal to 34.5 km. We can now readily determine the corresponding shorter-range bilinear comparison profile $\bar{c}_I^{(H)}(z)$. From Eqs. (1) and (3a),

$$\bar{c}_a = 2c_\mu - c_s, \tag{3b}$$

where

$$c_\mu = -(2z_b)^{-1}\{[(c_u^2+c_s^2-2c_a^2)g_u^{-1}]+[(2c_a^2-c_\ell^2-c_s^2)g_\ell^{-1}]\}. \tag{3c}$$

Values of all $\bar{c}_I^{(H)}(z)$ parameters appear in the third column of Table I. The profile $\bar{c}_I^{(H)}(z)$ is given by Eq. (2a), and is the dashed curve in Fig. (1a).

C. Ray geometry

Both the c(z) and $\bar{c}_I(z)$ profiles have the same numbers of received ray types for all ranges up to about R_c. As further indications of the close similarities between ray geometries associated with c(z) and its comparison bilinear profile, we present approximations for ray angles. The primary importance of these results is for the subsequent development of useful formulas for per-ray phase and amplitude differences. For surfaced S and R, we let S_N for $N > 1$ denote the SRBR ray which has N bottom reflections between S and R, and S_1, the BR ray. Our formulas for acoustic quantities, associated with varius rays in the case of S and R on the ocean surface, can be adapted to the cases with S and R on opposite boundaries if 2N is replaced by 2N - 1 for $N \geq 1$. Similarly, for the case of bottomed S and R, our formulas remain essentially the same if N is interpreted as the number of surface reflections between S and R.

Our first approximation is concerned with the initial angles, θ_{sN} and $\bar{\theta}_{sN}$, of rays S_N and $\bar{S}_N$, respectively, between surfaced S and R. All ray angles in this paper are measured positive clockwise from the x-axis, as displayed in Fig. 1(b) on the first half-lobes of rays S_N and $\bar{S}_N$. Using depth as the ray parameter, the range equations for S_N and $\bar{S}_N$ are[18]

$$R(\theta_{sN}) = 2N \int_0^{z_b} c(z)[c_s^2 \sec^2\theta_{sN} - c(z)^2]^{-\frac{1}{2}} dz \tag{4a}$$

and

$$\bar{R}(\bar{\theta}_{sN}) = 2N \int_0^{z_b} \bar{c}_I(z)[\bar{c}_s^2 \sec^2\bar{\theta}_{sN} - \bar{c}_I(z)^2]^{-\frac{1}{2}} dz. \tag{4b}$$

Combining Eqs. (4a) and (4b) for fixed range R, we have

$$F(\theta_{sN}) = \bar{R}(\bar{\theta}_{sN}) - R(\theta_{sN}) = 0. \tag{5}$$

Expanding $F(\theta_{sN})$ to linear terms about $\theta_{sN} = \bar{\theta}_{sN}$, and substituting the resulting expression in Eq. (5), we obtain

$$\theta_{sN} \doteq \bar{\theta}_{sN} - F(\bar{\theta}_{sN})/F'(\bar{\theta}_{sN}). \tag{6a}$$

After applying the weighted mean value theorem for integrals[19] to $F'(\theta_{sN})$, using Eq. (4a), and evaluating the resulting expression at $\theta_{sN} = \bar{\theta}_{sN}$, we have

$$F'(\bar{\theta}_{sN}) = [c_s^2 \sec^2\bar{\theta}_{sN} \tan\bar{\theta}_{sN}(c_s^2 \sec^2\bar{\theta}_{sN} - c_\nu^2)^{-1}]R, \tag{6b}$$

where $c_\nu = c(\nu)$ for some fixed ν such that $0 \leq \nu \leq z_b$. Using Eq. (4b) to evaluate $F(\bar{\theta}_{sN})$ and substituting Eq. (6b) in Eq. (6a), we arrive at

$$\theta_{sN} \doteq \bar{\theta}_{sN} - [1-(c_\nu^2/c_s^2)\cos^2\bar{\theta}_{sN}]\cot\bar{\theta}_{sN}(\Delta R/R), \tag{6c}$$

where

$$\Delta R \equiv R - R(\bar{\theta}_{sN}) \tag{6d}$$

and $R(\bar{\theta}_{sN})$ denotes the range equation for ray S_N evaluated at the initial angle for ray $\bar{S}_N$. To obtain upper and lower bounds for the magnitude of the angle correction in Eq. (6c), the second term on the right, we can simply set $c_\nu = c_a$ and $c_\nu = c_m \equiv \max(c_s, c_b)$, respectively. After approximating this second term by the average of the upper and lower approximations, we write

$$\theta_{sN} \doteq \bar{\theta}_{sN} + \gamma_N, \tag{7a}$$

where

$$\gamma_N \equiv -\{1-[c_a^2 + c_m^2)/2c_s^2]\cos^2\bar{\theta}_{sN}\}\cot\bar{\theta}_{sN}(\Delta R/R). \tag{7b}$$

Using, for example, the $c^{(H)}(z)$ and $\bar{c}_I^{(H)}(z)$ profiles described in Part B, we found that the right side of Eq. (6c) is an excellent approximation for all $N \geq 1$ and all ranges R up to about 40 km. For instance, we determined θ_{s1} using a numerical root-finding method on the $c^{(H)}(z)$ range equation[12] and $\bar{\theta}_{s1}$ from an explicit formula.[10] The numerical calculation for θ_{s1} agreed with the approximation of Eq. (7a) to at least five significant digits. Thus, $\bar{\theta}_{sN}$ closely approximates θ_{sN} for this example, as suggested in Fig. 1(b). Equation (6a) is expected to represent a good approximation for rays associated with other profiles in C, and we conclude that the initial angles for all rays associated with the c(z) and $\bar{c}_I(z)$ profiles are close for shorter ranges. The same conclusions can be shown to hold for other ray angles, such as those at the ocean bottom. Other approximations for relevant quantities involving the initial angles may be established readily using Eq. (7a). For example, an approximation required in Secs. II B and III B concerns the ratio of the tangents of the initial angles, given by

$$\tan\bar{\theta}_{sN}/\tan\theta_{sN} \doteq 1 + \xi_N, \tag{8a}$$

where

$$\xi_N \equiv - \gamma_N \tan\bar{\theta}_{sN} \csc^2\bar{\theta}_{sN}. \tag{8b}$$

We now present a second approximation for θ_{sN} which will be helpful in deriving qualitative information concerning per-ray amplitude differences in Sec. II B. It can be shown that the matching of average and surface sound speeds of c(z) and $\bar{c}_I(z)$ permits simplification of the quantity ΔR in Eq. (6d). If this simplification is inserted into γ_N in Eq. (7b), we obtain an approximation for θ_{sN}, which is valid for the shorter ranges where $\bar{c}_I(z)$ is useful, of the form

$$\theta_{sN} \doteq \bar{\theta}_{sN} + \Gamma_N, \tag{9a}$$

where

$$\Gamma_N \equiv - [z_b/(R/2N)] I_s \{1-[(c_a^2+c_m^2)/2c_s^2]\cos^2\bar{\theta}_{sN}\}\cot^4\bar{\theta}_{sN} \tag{9b}$$

and

$$I_s \equiv z_b^{-1} \int_0^{z_b} [\bar{c}_I(z)^2 - c(z)^2]/\bar{c}_s^2 dz. \tag{9c}$$

We remark that, since the sign of Γ_N depends only on the dimensionless constant I_s, Eq. (9a) can be used to determine whether θ_{sN} is greater or less than $\bar{\theta}_{sN}$ for shorter ranges. For our previous numerical comparison of $c^{(H)}(z)$ and $\bar{c}_I^{(H)}(z)$, for example, I_s has the positive value of 1.32×10^{-5}, so we conclude that $\bar{\theta}_{sN} > \theta_{sN}$, as shown in Fig. 1(b). This small numerical value of I_s is typical of other c(z) and $\bar{c}_I(z)$ profiles, although the sign of I_s may, of course, differ.

II. PER-RAY RESULTS: SHORTER RANGES

The source S is assumed to emit an omnidirectional cw signal proportional to $\sin(2\pi ft)$, where f is frequency in Hz. A ray will arrive at the receiver R in the form $A_N \sin[2\pi(ft - \phi_N)]$, where A_N is the relative amplitude owing to spreading and bottom losses (we neglect all other losses, including those due to attenuation and scattering). The phase ϕ_N (in cycles) is assumed to differ from that at the source because of travel time and phase shifts at boundary reflections. In this section we discuss per-ray phase and amplitude differences of rays associated with the c(z) and $\bar{c}_I(z)$ profiles, for an interval of shorter S-R ranges, where the latter profile yields positive sensitivity results.

A. Per-ray phase comparisons

The quantities τ_N and σ_N (or $\bar{\tau}_N$ and $\bar{\sigma}_N$) are travel times and phase shifts at each bottom reflection of rays associated with c(z) [or $\bar{c}_I(z)$]. We have

$$\phi_N = f\tau_N - [(N-1)/2] - N\sigma_N, \tag{10}$$

and similarly for $\bar{\phi}_N$, where the second term on the right side of Eq. (10) accounts for phase shifts at surface reflections. The expression for per-ray phase difference is

$$\Delta\phi_N \equiv \phi_N - \bar{\phi}_N = f(\tau_N - \bar{\tau}_N) - N(\sigma_N - \bar{\sigma}_N). \tag{11}$$

In Sec. IC we showed that the values of bottom angles of rays associated with c(z) and $\bar{c}_I(z)$ are very close. Since the bottom sound speeds of c(z) and $\bar{c}_I(z)$ are matched, we can approximate $\Delta\phi_N$ by

$$\Delta\phi_N \doteq f(\tau_N - \bar{\tau}_N) \equiv f\Delta\tau_N. \tag{12}$$

As a numerical illustration, we computed $\Delta\phi_N$ for rays associated with the $c^{(H)}(z)$ and $\bar{c}_I^{(H)}(z)$ profiles using Eqs. (11) and (12) and Rayleigh reflec-

tion theory.[20] (References 10 and 12 provide the relevant travel-time formulas, and bottom parameter values are given in Sec. II B.) For a source frequency of 200 Hz and for ranges up to about 69 km, Eqs. (11) and (12) differed very little, at most in the third significant figure. The close match between Eqs. (11) and (12) is not expected to depend on the particular bottom-interaction model selected.

We next derive an important approximation for $\Delta\phi_N$ in Eq. (12), which enables us to determine readily a range interval on which all per-ray phases associated with $c(z)$ and $\bar{c}_I(z)$ correspond closely. Let δ be the dimensionless quantity defined by $\delta \equiv (c_a - \bar{c}_a)c_s^{-1}$, one measure of the difference between the $c(z)$ and $\bar{c}_I(z)$ profiles. Since δ is small and ray geometries for $c(z)$ and $\bar{c}_I(z)$ are very close, we can find an approximation for the travel-time difference from Ref. 21. We note the identity

$$c(z) = c_s\{\bar{c}_I(z)c_s^{-1} + \delta[c(z)-\bar{c}_I(z)](c_a-\bar{c}_a)^{-1}\}, \tag{13a}$$

choose $\bar{c}_I(z)$ as the unperturbed state in the formalism of Ref. 21, and apply Eq. (13a) and a depth ray parametrization to Eq. (9) of Ref. 21 to obtain

$$\Delta\tau_N \doteq 2N\int_0^{z_b} [\bar{c}_I(z)-c(z)]\bar{c}_I(z)^{-2}\{1-[\bar{c}_I(z)/\bar{\beta}_N]^2\}^{-\frac{1}{2}}dz, \tag{13b}$$

where $\bar{\beta}_N$ is the Snell's law constant for ray $\bar{S}_N$. For our purpose we found it convenient to specify $\bar{\beta}_N$ by

$$\bar{\beta}_N = \bar{c}_\mu \sec\bar{\theta}_{\mu N}, \tag{14a}$$

where $\bar{c}_\mu$ is given by Eq. (1a) and $\bar{\theta}_{\mu N}$ is the angle along the ray $\bar{S}_N$ which corresponds to the value $\bar{c}_\mu$. Using the identity

$$\bar{c}_I(z) = \bar{c}_\mu[1+\bar{\epsilon}(z)], \tag{14b}$$

where

$$\bar{\varepsilon}(z) \equiv [\bar{c}_I(z)-\bar{c}_\mu]\bar{c}_\mu^{-1}, \tag{14c}$$

and substituting Eqs. (14) into the denominator of the integrand of Eq. (13b), we may write

$$\Delta\tau_N \doteq 2N\int_0^{z_b}[\bar{c}_I(z)-c(z)]\{\bar{c}_\mu[1+\bar{\varepsilon}(z)]\}^{-2}(1-\{\cos\bar{\theta}_{\mu N}[1+\bar{\varepsilon}(z)]\}^2)^{-\frac{1}{2}}dz. \tag{15}$$

By expanding the integrand in Eq. (15) as a Maclaurin series in $\bar{\varepsilon}$, noting that the leading term vanishes because of the equal average sound speeds of $c(z)$ and $\bar{c}_I(z)$, and using Eq. (12) we obtain the key approximate formula

$$\Delta\phi_N \doteq 2N(fz_b/\bar{c}_\mu)I_\mu\, G(\bar{\theta}_{\mu N}), \tag{16a}$$

where

$$I_\mu \equiv z_b^{-1}\int_0^{z_b}[\bar{c}_I(z)^2-\bar{c}_I(z)c(z)]/\bar{c}_\mu^2\,dz \tag{16b}$$

and

$$G(\bar{\theta}_{\mu N}) \equiv (1-3\sin^2\bar{\theta}_{\mu N})/\sin^3\bar{\theta}_{\mu N}. \tag{16c}$$

In order to locate those ranges where $\bar{\phi}_N$ closely approximates ϕ_N, we first use Eq. (16a), a much simpler expression than Eq. (12), to describe the qualitative behavior of $\Delta\phi_N$. For fixed N and increasing R, it follows from the behavior of G in Eq. (16c) that if I_μ is positive (or negative), then $\Delta\phi_N$ is an increasing (or decreasing) function of range, from negative (or positive) through zero to positive (or negative) values. Moreover, it can be shown using Eq. (16a) [or Eq. (11)] and Eqs. (4) that $\Delta\phi_N$ is equal to a product of N and a function of N/R. This implies that the zeros of $\Delta\phi_N$ as N varies are equally spaced in range; i.e., that $\Delta\phi_N(NR_1) = 0$, where R_1

denotes the range at which $\Delta\phi_1$ vanishes. In order to avoid near-source effects, we do not consider ranges which are less than, say, 1 km. It follows from Eq. (16a) that for $1 \leq R \leq R_1$, the $\Delta\phi_N$ are all of the same sign, and, for a fixed N, $|\Delta\phi_N|$ achieves its maximum value at 1 km. Finally, we note that for very short ranges, $|\Delta\phi_N|$ increases in a manner proportional to N.

To illustrate the qualitative behavior of $\Delta\phi_N$ and the accuracy of the approximation Eq. (16a), we computed per-ray phase differences associated with the $c^{(H)}(z)$ and $\bar{c}_I^{(H)}(z)$ profiles from 1 km up to about R_c = 69 km. The source frequency for our examples is 200 Hz, and the rays with significant amplitudes at these ranges, as determined in the next subsection, are N = 1 to 4. We display in Fig. 2 the graphs of $\Delta\phi_1$, $\Delta\phi_2$, and $\Delta\phi_3$ up to about 30 km. The solid (or dashed) curves describe exact (or approximate) per-ray phase differences which are computed using Eq. (11) [or Eq. (16a]. These curves indicate that $\Delta\phi_N$ for all N is small up to about 20 km. We note the generally high accuracy of the Eq. (16a) approximation to Eq. (11), in this case for which $I_\mu (= 8.05 \times 10^{-6})$ is positive. All curves in Fig. 2, as well as numerical calculations up to R_c, show that $\Delta\phi_N$ increases from negative to positive values as R increases, for all N. Finally, we note that the previously described qualitative behaviour of $\Delta\phi_N$ at ranges less than R_1 = 14.3 km is illustrated in Fig. 2. For instance, at ranges less than 4 km, $|\Delta\phi_N|$ increases in a manner which is proportional to N.

Since $\Delta\phi_N$ is predicted by Eq. (16a) to vanish at some range, it follows that, for each N and for some range interval, ϕ_N and $\bar{\phi}_N$ correspond very closely. On the other hand, $|\Delta\phi_N|$ gets unacceptably large for sufficiently long ranges. This growth obviously becomes most severe for the

BR (N = 1) rays well before any SRBR rays (with N > 1), as can be observed in Fig. 2. We use this fact to determine a maximum range value, R_I^P, for which the per-ray phases of all rays associated with $\bar{c}_I(z)$ acceptably approximate those of c(z). Let q_p be a phase tolerance. To determine R_I^P, we take N = 1 and $R > R_1$ in Eq. (16a) and set

$$|\Delta\phi_1| = q_p. \tag{17}$$

The monotonicity of $\Delta\phi_N$ guarantees that there is a unique value R_I^P which solves Eq. (17) and which increases with q_p. Letting α be defined by $\alpha \equiv 2[(fz_b)/\bar{c}_\mu]|I_\mu|q_p^{-1}$ and $\bar{X} \equiv \sin\bar{\theta}_{\mu 1}$, noting that $0 < \bar{X} < \sqrt{3}/3$ corresponds to $R > R_1$, and substituting α and $\bar{X}$ into Eq. (17), then we obtain

$$\bar{X}^3 + 3\alpha\bar{X}^2 - \alpha = 0. \tag{18a}$$

For $0 < \alpha < \frac{1}{2}$, we note that the solution $\bar{X}_1$ to Eq. (18a) takes the form[22]

$$\bar{X}_1 = \alpha^{\frac{1}{3}}\{[\tfrac{1}{2}-\alpha^2+(\tfrac{1}{4}-\alpha^2)^{\frac{1}{2}}]^{\frac{1}{3}} + [\tfrac{1}{2}-\alpha^2-(\tfrac{1}{4}-\alpha^2)^{\frac{1}{2}}]^{\frac{1}{3}}\} - \alpha. \tag{18b}$$

We combine the solution $\bar{X}_1$ to Eq. (18a) with the range equation[10] for the BR ray associated with $\bar{c}_I(z)$ to determine the upper range limit R_I^P,

$$R_I^P = 2[(\bar{g}_\ell^{-1} + \bar{g}_u^{-1})(\bar{\beta}_1^2 - \bar{c}_a^2)^{\frac{1}{2}} - \bar{g}_\ell^{-1}(\bar{\beta}_1^2 - \bar{c}_b^2)^{\frac{1}{2}} + \bar{g}_u^{-1}(\bar{\beta}_1^2 - \bar{c}_s^2)^{\frac{1}{2}}], \tag{19a}$$

where

$$\bar{\beta}_1 = \bar{c}_\mu(1-\bar{X}_1^2)^{-\frac{1}{2}}. \tag{19b}$$

For the determination of a lower range limit R_L, the phase tolerance q_L should be chosen more strictly than q_p (for example, $q_L = q_p/2$), because of the previously mentioned fact that $|\Delta\phi_N|$ increases with N for very short ranges. Since $|\Delta\phi_1|$ achieves its maximum value at 1 km for ranges less than R_1, the method for the computation of R_L is as follows: if

$|\Delta\phi_1|$ at R = 1 km is less than or equal to q_L, choose R_L = 1 km; otherwise, set $|\Delta\phi_1| = q_L$ and compute R_L in exactly the same manner as R_I^P.

Given any profile c(z) in C, we have developed a straightforward, analytical procedure using Eq. (16a) for determining a range interval $[R_L, R_I^P]$ in which the per-ray phases associated with $\bar{c}_I(z)$ approximate acceptably well those associated with c(z). We illustrate this interval by means of the $c^{(H)}(z)$ and $\bar{c}_I^{(H)}(z)$ profiles. For the upper (and lower) phase tolerance, we select q_p = 0.05 cycles (and q_L = 0.025 cycles) and use our procedure to find that, for a source frequency of 200 Hz, $[R_L, R_I^P]$ = [1 km, 20.0 km]. Since the dashed $\Delta\phi_1$ curve has been computed in this example, range intervals corresponding to these and other tolerance levels may also be obtained graphically from Fig. 2. That is, R_I^P is that range greater than R_1 which corresponds to the ordinate value $|\Delta\phi_1| = q_p$, and R_L is obtained similarly. Finally, we remark that, although $\Delta\phi_1$ associated with the BR rays continues to grow rapidly for $R > R_I^P$ in this particular example, the $\Delta\phi_N$ for N > 1 remain small for a significant range interval beyond R_I^P. This feature, of having only a single dramatically growing per-ray phase difference, can be shown by our qualitative discussion to apply to other profiles in C, and leads to an extension of positive per-ray phase sensitivity results to longer ranges in Sec. III.

B. Per-ray amplitude comparisons

To compare amplitude differences between corresponding rays associated with a c(z) profile and its bilinear counterpart $\bar{c}_I(z)$, we first develop an approximation analogous to that of Eq. (16a) for phase. For any ray S_N, the amplitude at the receiver relative to that at a unit distance from the source is given by

$$A_N = (B_N)^N (I_0/I_x)_N^{-\frac{1}{2}} \tag{20}$$

and similarly for $\bar{A}_N$, where $(I_0/I_x)_N$ and B_N represent the geometric spreading loss and loss per bottom reflection. We shall neglect differences in bottom losses of rays S_N and $\bar{S}_N$ for the same reasons, i.e., very close bottom angles and equal bottom sound speeds, that we neglected bottom phase-shift differences previously. We also ignore differences in the Snell's law constants $\beta_N = c_s \sec\theta_{sN}$ and $\bar{\beta}_N = \bar{c}_s \sec\bar{\theta}_{sN}$ here, another very good approximation which is based on the fact that $\bar{c}_s = c_s$ and results of Sec. IC. After computing the geometric spreading losses[23] and invoking our approximations, we have

$$A_N/\bar{A}_N \doteq (\tan\bar{\theta}_{sN}/\tan\theta_{sN}) Y^{\frac{1}{2}}, \tag{21a}$$

where

$$Y \equiv \left(\int_0^{z_b} \bar{c}_I(z)\{1-[\bar{c}_I(z)/\bar{\beta}_N]^2\}^{-\frac{3}{2}} dz\right)\left(\int_0^{z_b} c(z)\{1-[c(z)/\bar{\beta}_N]^2\}^{-\frac{3}{2}} dz\right)^{-1}. \tag{21b}$$

If we substitute the identity

$$c(z) = c_s[1+\Delta(z)], \tag{22a}$$

where

$$\Delta(z) \equiv [c(z)-\bar{c}_s]\bar{c}_s^{-1}, \tag{22b}$$

and similar ones for $\bar{c}_I(z)$ and $\bar{\Delta}(z)$, into the denominator of the integrand of Eq. (21b), retain linear terms in $\Delta(z)$ and $\bar{\Delta}(z)$, and use the equal average sound speeds of $c(z)$ and $\bar{c}_I(z)$, we find

$$Y^{\frac{1}{2}} \doteq [(1+\bar{y})/(1+y)]^{\frac{1}{2}} \tag{23a}$$

where

$$y \equiv 3\cot^2\bar{\theta}_{sN}\{z_b^{-1} \int_0^{z_b} [c(z)/\bar{c}_\mu]\Delta(z)\,dz\}, \tag{23b}$$

and similarly for $\bar{y}$. Then, if we expand the right side of Eq. (23a) in a Taylor series about $(y,\bar{y}) = (0,0)$ and substitute this expansion and Eq. (8a) into Eq. (21a), we obtain an approximation for $A_N/\bar{A}_N$ in the form

$$A_N/\bar{A}_N \doteq 1+\eta_N, \tag{24a}$$

where

$$\eta_N \equiv \xi_N+\zeta_N, \tag{24b}$$

$$\zeta_N \equiv K_s \cot^2\bar{\theta}_{sN}, \tag{24c}$$

$$K_s \equiv \frac{3}{2}(\bar{c}_s/\bar{c}_\mu) I_s, \tag{24d}$$

and ξ_N and I_s are given by Eqs. (8b) and (9c), respectively. For any specific $c(z)$ and $\bar{c}_I(z)$ profiles, K_s is a constant which we anticipate is small in magnitude because I_s is small. For example, in the case of the $c^{(H)}(z)$ and $\bar{c}_I^{(H)}(z)$ profiles, $K_s = 2.02 \times 10^{-5}$. We easily establish from Eq. (24a) the important approximation for the per-ray amplitude anomaly ΔL_N (in dB),

$$\Delta L_N \equiv 20 \log_{10}(A_N/\bar{A}_N) \doteq d\eta_N, \tag{25}$$

where $d = 20/(\log_e 10) = 8.69$. It can be shown that the approximation in Eq. (25) is close for all N and for somewhat longer ranges than that in Eq. (16a).

We use the convenient approximation of Eq. (25) to specify those ranges where A_N and $\bar{A}_N$ correspond closely for all N. At very short ranges (i.e., very steep initial angles), Eq. (25) shows that all per-ray amplitude anomalies are negligible, so that we can choose the minimum range for which A_N and $\bar{A}_N$ correspond closely as 1 km. Turning next to a determination of a corresponding maximum range, we note certain qualitative

features of ΔL_N. It can be shown with the aid of Eq. (9a) that ξ_N and ζ_N, which appear in Eq. (25), both depend in the same way on the sign of I_s. Therefore, for all N and any R, ΔL_N is of the same sign as I_s. If we fix R and vary N, then ξ_N and ζ_N will be greatest in magnitude for the ray with the most shallow initial angle. Since ξ_N and ζ_N are both of the same sign, we conclude that for a fixed range, the greatest per-ray amplitude anomaly predicted by Eq. (25) occurs for the (BR) N = 1 rays. If we fix N and vary R, then by similar reasoning $|\Delta L_N|$ is an increasing function of range. Insofar as these qualitative features of ΔL_N depend on Eq. (9a), they are certainly valid for the ranges where $R \leq R_I^P$, but in fact they are often true for longer ranges as well. From these qualitative results, we base the determination of a maximum range limit R_I^A on the BR rays. Given a per-ray amplitude tolerance q_A, we determine R_I^A via Eq. (25) by setting $|\Delta L_1| = q_A$. Since $|\Delta L_1|$ is an increasing function of range, there is a unique value of R_I^A which solves this equation and increases with q_A. Therefore, $\bar{A}_N$ approximates A_N acceptably well for all N for ranges in the interval $[1, R_I^A]$.

Since we have two upper limits R_I^P and R_I^A for application of the $\bar{c}_I(z)$ comparison profile, the question naturally arises as to which value is smaller and thus more restrictive. We next present convincing numerical evidence that even for moderately small values of q_A, R_I^A is typically much greater than R_I^P. We computed ΔL_N associated with the $C^{(H)}(z)$ and $\bar{c}_I^{(H)}(z)$ profiles using both the exact formulas in Eq. (20), which include bottom losses, and the approximation Eq. (25). Rayleigh reflection theory was used as the bottom loss model, with numerical values[12] of 1757.17 ms^{-1} for the ocean bottom sound speed and 0.525 (and 0.877) for the ratio of water to bottom densities (and sound speeds). If we employ a typical

criterion that a ray with N bounces is significant if $A_N/A_1 \geq 0.01$, then for the $c^{(H)}(z)$ and $\bar{c}_I^{(H)}(z)$ profiles, this condition is satisfied for all rays $N \leq 4$ up to about $R_c = 69$ km. For this example, the solid (and dashed) curves in Fig. 3 represent the exact (and approximate) per-ray amplitude anomalies, in dB, for the N = 1 and 2 rays for ranges up to 45 km. The N = 3 and 4 curves are not displayed because their anomalies are extremely small. An important result from Fig. 3 is that the per-ray amplitude anomalies for all rays are insignificant, not only up to $R_I^P = 20$ km but also up to and well beyond 45 km as well. In addition, the dashed-curve approximations are very close to the solid curves for all ranges in Fig. 3. There is a sharp increase in the solid N = 1 (and N = 2) curve, followed by a discontinuity, at a range of about 16.5 km (and 33.1 km), where the bottom angles of the N = 1 (and N = 2) rays approach their critical values in Rayleigh reflection theory. Although for each N the ranges associated with the critical bottom angles of corresponding rays are close, they are not exactly equal. The particular Rayleigh bottom-loss model used in our calculations for the solid curves in Fig. 3 overmagnifies the bottom-loss differences at these ranges, and, consequently, the per-ray amplitude anomalies. A more refined bottom-interaction model would not be expected to produce such conspicuous differences. With the exception of these features due to the bottom-interaction model, we note that Fig. 3 illustrates all the qualitative variations of ΔL_N with N and R discussed above for the case of I_s positive. For instance, for each N, ΔL_N is positive and increases with range, while for each R, $|\Delta L_N|$ decreases with N. Selecting q_A to be 0.4 dB, we find that R_I^A is equal to 52.2 km, a substantially larger value than $R_I^P = 20.0$ km in this example. If we define $R_I = \min(R_I^P, R_I^A)$, then all per-ray phases and relative amplitudes associated with c(z) and $\bar{c}_I(z)$ are

acceptably close for the shorter ranges in the interval $[R_L, R_I]$. Although it is a simple matter to consider either the case of $R_I = R_I^P$ or that of $R_I = R_I^A$, based on our numerical examples we shall restrict ourselves hereafter to the highly probable case that $R_I = R_I^P$.

With the procedure specified for determining the shorter-range interval $[R_L, R_I]$ for the case of S and R on the ocean surface, results for other source-receiver boundary locations follow readily. We note first that the key formulas Eqs. (16a) and (25) for the case of surfaced S and R can be adapted without essential change to the other cases. Second, the crucial role of phase and amplitude differences between the BR rays for surfaced S and R is replaced by those between the SR (or D) rays for S and R on the bottom (or on opposite boundaries). For simplicity here, we consider only the highly probable occurrence that per-ray phase differences alone determine the shorter-range intervals. If S and R are both located on the ocean bottom, then Eq. (16a) holds if N is interpreted as the number of surface reflections. Thus, the shorter-range interval is exactly the same as $[R_L, R_I]$ for surfaced S and R. Similar reasoning shows that the travel-time difference for the D rays at range R/2 is exactly half that of both the BR and SR rays at range R. We can then argue that if S and R are on opposite boundaries, the size of the shorter-range interval is more than half the size of $[R_L, R_I]$, extending from less than $\max(1, R_L/2)$ to more than $R_I/2$. This interval is the same whether S is on the surface and R is on the bottom, or vice-versa. Therefore, determination of the range interval for acceptable correspondence between per-ray quantities associated with the two sound-speed profiles can be effected for any near-boundary locations of S and R.

III. PER-RAY RESULTS: LONGER RANGES

A. Comparison Profile

The main difficulty in extending the close correspondence of per-ray acoustic quantities, associated with the c(z) and $\bar{c}_I(z)$ profiles, to ranges longer than R_I is the unacceptably large values of $\Delta\phi_1$. However, we recall that there is one range value R_1, which is less than R_I, for which $\Delta\phi_1$ vanishes. This suggests that at a range $R > R_I$, a slight perturbation of the $\bar{c}_I(z)$ profile could perhaps shift R_1 to coincide with R. This idea motivates a scheme to construct a different bilinear comparison profile for each range $R > R_I$. We indicate members of the family of bilinear comparison profiles, one for each range, by $\bar{c}_{II}(z)$.

For a specific c(z) profile and range $R > R_I$, the parameters of the $\bar{c}_{II}(z)$ profile are determined as follows:

(1) The phases of the BR (or N = 1) rays for the two profiles are set equal;

(2) the depth-averaged sound speeds of the two profiles are set equal:

(3) the difference between the surface and bottom sound speeds of $\bar{c}_{II}(z)$ is equal to that of c(z), i.e.,

$$\bar{c}_b - \bar{c}_s = c_b - c_s; \tag{26a}$$

(4) the SOFAR-axis depths of the profiles are equal, i.e.,

$$\bar{z}_a = z_a. \tag{26b}$$

We note that SR (or D) is substituted for BR in condition (1) in order to specify the $\bar{c}_{II}(z)$ profile for S and R on the ocean bottom (or on opposite

boundaries). Also, conditions (2) and (4) were selected for the same reasons as in the construction of the $\bar{c}_I(z)$ profile in Sec. IB, and condition (3) is weaker than that used for $\bar{c}_I(z)$ in order to permit imposition of condition (1). Finally, we remark that our construction procedure identifies important information for the selection or specification of a c(z) profile at longer ranges. Condition (1) identifies the phase of the ray with the largest amplitude as significant , while conditions (2) - (4) identify the same critical aspects of the profile data as those noted earlier for shorter ranges.

Condition (2) is given by Eq. (1a) with $\bar{c}_{II}(z)$ written in place of $\bar{c}_I(z)$. If Eqs.(26a) and (26b) are substituted in Eq. (1b), then an expression for $\bar{c}_a$ of the $\bar{c}_{II}(z)$ profile is obtained:

$$\bar{c}_a = [(c_b - c_s) z_b^{-1}] z_a + 2c_\mu - \bar{c}_s - (c_b - c_s). \tag{26c}$$

We recognize from Eqs. (26) that $\bar{z}_a$, $\bar{c}_b$, and $\bar{c}_a$ depend only on $\bar{c}_s$ and known c(z) parameters. Moreover, for a fixed $R > R_I$ and a given c(z) profile, the phase ϕ_1 of the BR ray associated with c(z) can be calculated analytically or numerically. Therefore, $\bar{c}_s$ can be determined by condition (1):

$$\Delta\phi_1(\bar{c}_s) = \phi_1 - \bar{\phi}_1(\bar{c}_s) = 0, \tag{27}$$

where the other bilinear profile parameters are regarded as functions of $\bar{c}_s$ only. The formula for $\bar{c}_{II}(z)$ is then given by Eqs. (2) with $\bar{c}_s$ and $\bar{c}_b$ written in place of c_s and c_b. Eq. (27) is assumed to have a solution $\bar{c}_s$ close to c_s, which we have verified by analysis which will not be presented here. We regard $\bar{c}_s$ to be close to c_s if

$$|(c_s - \bar{c}_s)/(c_s - \bar{c}_a)| \ll 1. \tag{28}$$

From Eqs. (26a), (26c), and (28), it follows that $\bar{c}_b$ is close to c_b and that the SOFAR-axis sound speeds of the $\bar{c}_I(z)$ and $\bar{c}_{II}(z)$ profiles are close. Therefore, the $\bar{c}_{II}(z)$ profile at each longer range can be regarded as a small perturbation of the $\bar{c}_I(z)$ profile for the given $c(z)$ in C.

The solution $\bar{c}_s$ of Eq. (27) varies in a complicated manner with range, because $\bar{c}_s$ is close to c_s while simultaneously $\Delta\phi_1(c_s)$ was shown in Sec. IIA to increase significantly at longer ranges. We therefore propose that Eq. (27) be solved numerically for each $R > R_I$ using Eq. (12), i.e., using exact travel-time formulas. Thus, Eq. (27) becomes

$$\bar{\tau}_1(\bar{c}_s) = \tau_1, \tag{29}$$

where τ_1 is known and $\bar{\tau}_1(\bar{c}_s)$ can be found in Ref. 10. Bottom phase-shift differences are neglected in Eq. (29) for the same reasons they were omitted in Sec. IIA. We have found that Newton's method[24] for solving Eq. (29) is adequate for speed and high accuracy, and that c_s provides an acceptable initial estimating value for $\bar{c}_s$. We note that Eq. (29) and its analogues for other source-receiver boundary locations only contain travel times. By arguments similar to those given at the end of Sec. II, we conclude that the $\bar{c}_{II}(z)$ profile for $R > R_I$ is exactly the same for S and R on the surface as for S and R on the bottom. Similarly, we conclude that the $\bar{c}_{II}(z)$ profile for R more than $R_I/2$ is exactly the same for S on the surface and R on the bottom, as for S on the bottom and R on the surface.

We have determined that $\bar{c}^{(H)}_{II}(z)$ profile from the $c^{(H)}(z)$ profile for ranges greater than R_I = 20 km up to about R_c = 69 km. The value of $\bar{c}_s$ for the $\bar{c}^{(H)}_{II}(z)$ profile varies between a minimum of 1540.05 ms^{-1} and a maximum of 1540.86 ms^{-1}. This indicates that $\bar{c}_s < c_s$ (=1541.50 ms^{-1}) in this example for all $R > R_I$. For all values of $\bar{c}_s$, the left side of Eq. (28) is less than 0.027,

so we conclude that $\bar{c}_s$ is close to c_s for the $\bar{c}_{II}^{(H)}(z)$ profile when $R_I < R < R_c$. Since $c_b = c_s$ for our particular example $c^{(H)}(z)$ profile, $\bar{c}_b = \bar{c}_s$ for the $\bar{c}_{II}^{(H)}(z)$ profile. The value of $\bar{c}_a$, computed from Eq. (26c), varies between a minimum of 1482.54 ms^{-1} and a maximum of 1483.35 ms^{-1}. Thus, at any range, the graph of $\bar{c}_{II}^{(H)}(z)$ is very close to that of the $\bar{c}_I^{(H)}(z)$ profile displayed in Fig. (1a).

As we noted, condition (3) is weaker than the corresponding requirement imposed on the $\bar{c}_I(z)$ profile. However, it is sufficient to guarantee an equal number of received rays of identical type for the two c(z) and $\bar{c}_{II}(z)$ profiles, for ranges up to about R_c. Moreover, the formulas in Eqs. (7a) and (8a), which apply without modification to the c(z) and $\bar{c}_{II}(z)$ profiles, represent good approximations at longer ranges. We conclude that the geometry and angles of corresponding rays associated with the c(z) and $\bar{c}_{II}(z)$ profiles can be shown to be very close for all source-receiver boundary locations. The verification of this important result proceeds as in Sec. IC, so we omit the details here.

B. Per-ray comparisons

We recall from subsection A that the difference $\Delta\phi_1$ between the phases of the (BR) N = 1 rays for the c(z) and $\bar{c}_{II}(z)$ profiles is identically zero when $R > R_I$. We now present approximations to $\Delta\phi_N$, $N \geq 2$, and use them to demonstrate that these phase differences remain acceptably small over a substantial range interval beginning at R_I and ending at some range R_{II}^P. Since we found $\bar{c}_{II}(z)$ to be a small perturbation off $\bar{c}_I(z)$, the discussion in Sec. IIA of $\Delta\phi_N$ can be applied here with minor modifications. Specifically, the assumptions and expansions used to derive Eq. (16a) are easily seen to hold for $N \geq 2$ in a longer range context, so that

$$\Delta\phi_N \doteq 2N[(fz_b)/\bar{c}_a]\ I_a\ G(\bar{\theta}_{aN}),\quad N \geq 2, \tag{30a}$$

where

$$I_a \equiv z_b^{-1} \int_0^{z_b} [\bar{c}_{II}(z)^2 - \bar{c}_{II}(z)c(z)]/\bar{c}_a^{\,2}\,dz \tag{30b}$$

and

$$G(\bar{\theta}_{aN}) \equiv (1-3\sin^2\bar{\theta}_{aN})/\sin^3\bar{\theta}_{aN}. \tag{30c}$$

The quantity $\bar{\theta}_{aN}$ in Eqs. (30a) and (30c) designates the angle of the Nth ray at the SOFAR axis associated with $\bar{c}_{II}(z)$. All the conclusions in Sec. IIA concerning the qualitative behavior of $\Delta\phi_N$ for $N \geq 2$ can also be shown to hold here for $R > R_I$ via Eq. (30a). For instance, if I_a is positive (or negative), then for a fixed $N \geq 2$, $\Delta\phi_N$ increases (or decreases) from negative (or positive) values through zero to large positive (or negative) values. We also conclude from Eq. (30a) that $|\Delta\phi_N|$ gets large at sufficiently long ranges for any given N, and that the growth becomes most severe for the N = 2 rays well before any rays with N > 2. This implies that given some phase tolerance, such as q_p which was used to specify R_I^p, the determination of the range R_{II}^p should be based on the N = 2 rays. Specifically, R_{II}^p is found among the ranges beyond which $\Delta\phi_2$ vanishes and is that range at which $|\Delta\phi_2| = q_p$, where $\Delta\phi_2$ is given by Eq. (30a).

To illustrate our results and the accuracy of Eq. (30a), we computed per-ray phase differences associated with the $c^{(H)}(z)$ and $\bar{c}_{II}^{(H)}(z)$ profiles from R_I = 20 km up to about R_c = 69 km. The rays with significant amplitudes at these ranges are, as in Sec. II, N = 1 to 4. We display in Fig. 4 graphs of $\Delta\phi_N$ for N = 1 to 3 from 20 to 52 km. The solid curves give exact values

of $\Delta\phi_N$ computed from Eq. (11) as described in Sec. IIA, while the dashed curves give approximate values, determined from Eq. (30a), of $\Delta\phi_N$ for N = 2 and 3. The qualitative behavior described previously for $\Delta\phi_N$ is illustrated in Fig. 4 for a case where I_a in Eq. (30a) is positive. All curves in Fig. 4 as well as calculations for $\Delta\phi_4$ show that $|\Delta\phi_N|$ for each $N \geq 1$ is small for a substantial range interval beginning at R_I. The approximations for $N \geq 2$ are seen to be very close over all ranges shown. It is important to stress that there is a significant drop in magnitude of $\Delta\phi_N$ for all N and $R > R_I$ when the $\bar{c}^{(H)}_{II}(z)$ comparison profile is used in place of the $\bar{c}^{(H)}_{I}(z)$ comparison profile. The biggest decrease, of course, occurs for N = 1 because of the construction of the $c^{(H)}_{II}(z)$ profile, but the decrease in magnitude is noteworthy for $N \geq 2$ as well. These trends can be appreciated by comparing the relatively smaller values of $\Delta\phi_N$ in Fig. 4, for 20 to 30 km, to those in Fig. 2. Using the same value of 0.05 cycles for q_p as in Sec. IIA, we find that R^P_{II} = 45.2 km for this example. Therefore, for our selected tolerance and a source frequency of 200 Hz, the comparison profile $c^{(H)}_{II}(z)$ provides acceptable per-ray phase approximations to $c^{(H)}(z)$ for ranges in the interval $(R_I, R^P_{II}]$ = (20 km, 45.2 km].

We next briefly discuss the determination of a range interval $(R_I, R^A_{II}]$, in which all amplitudes associated with corresponding rays of the c(z) and $\bar{c}_{II}(z)$ profiles agree closely. Again, because $\bar{c}_{II}(z)$ is a small perturbation off $\bar{c}_I(z)$, the formulas of Eqs. (24) and (25) for $A_N/\bar{A}_N$ and ΔL_N, $N \geq 1$, can be applied here. It can be shown that for each value of N, the range of validity of these approximations generally includes those ranges where ΔL_N is small. As in Sec. IIB, the determination of R^A_{II} should be based on the N = 1 rays, which typically display the largest per-ray amplitude anomaly for $R > R_I$. Thus,

if q_A is the amplitude tolerance (in dB), we determine R_{II}^A as the range at which $|\Delta L_1| = q_A$, where ΔL_1 is given by Eq. (25).

We computed per-ray amplitude anomalies for rays associated with the $c^{(H)}(z)$ and $\bar{c}_{II}^{(H)}(z)$ profiles. The solid curves in Fig. 5 give exact values of ΔL_N (in dB), for N = 1 to 3 and 20 km $\leq R \leq$ 52 km, including bottom losses and calculated as described in Sec. IIB. These curves indicate that for all N in this example, ΔL_N is small for a significant range interval beginning at R_I. The cause for the increases, followed by discontinuities in the N = 2 and 3 solid curves, is the same as that given for Fig. 3. The dashed curves in Fig. 5 are approximations for ΔL_N, computed using the analogue of Eq. (25) for $R > R_I$. The approximation for ΔL_1 is quite good from 20 km to 40 km and fairly good from 40 km to 45 km. The N = 2 (and N = 3) dashed curve is a good approximation from 20 km to 33.1 (and 49.7) km, in which interval bottom losses occur, and is an excellent approximation from 33.1 (and 49.7) km to 52 km, where there are no bottom losses. Thus, the difference in accuracy of these approximations as range varies is consistent with the fact that the difference in bottom losses for the two profiles is neglected in Eq. (25). We note that all dashed curves in Fig. 5 display the same qualitative features as the dashed curves in Fig. 3; i.e., they increase with range, and for a fixed range, they decrease as N increases. Using, for example, the tolerance q_A = 0.4 dB, it follows that R_{II}^A = 45.4 km for the $c^{(H)}(z)$ and $\bar{c}_{II}^{(H)}(z)$ profiles.

We define $R_{II} = \min(R_{II}^P, R_{II}^A)$ and conclude that all per-ray phases and amplitudes associated with a $\bar{c}_{II}(z)$ profile acceptably approximate their counterparts for a c(z) profile at any range in the interval $(R_I, R_{II}]$. In our numerical example, for a source frequency of 200 Hz and our selected tolerances, $(R_I, R_{II}]$ = (20.0 km, 45.2 km]. The extension of our results to other boundary

locations of S and R proceeds in a similar fashion to that indicated at the end of Sec. II. In particular, recalling that the $\bar{c}_{II}(z)$ profile for $R > R_I$ is the same for bottomed S and R as for surfaced S and R, we conclude that $(R_I, R_{II}]$ is the same interval in these two cases. Similarly, if S and R are located on opposite boundaries, the longer range intervals are the same. extending from more than $R_I/2$ to more than $R_{II}/2$. In summary (when S and R are located on the same boundary), we define for any c(z) profile its overall bilinear comparison profile as

$$\bar{c}(z) = \begin{cases} \bar{c}_I(z) \quad , & R_L \leq R \leq R_I \quad , \\ \bar{c}_{II}(z) \quad , & R_I < R \leq R_{II} \quad . \end{cases} \tag{31}$$

For any given range in $[R_L, R_{II}]$ this simpler profile $\bar{c}(z)$ has per-ray phases and amplitudes which agree, to within specified tolerances, with those of corresponding rays associated with the given profile.

IV. TOTAL FIELD

In this section we investigate the total-field phase and amplitude differences for ranges in $[R_L, R_{II}]$, associated with the c(z) and $\bar{c}(z)$ profiles. With a source emitting an omnidirectional cw signal, the total field at the receiver associated with a c(z) profile is

$$A\sin[2\pi(ft-\Phi)] = \sum_{N=1}^{N_{max}} A_N \sin[2\pi(ft-\phi_N)], \tag{32}$$

and similarly with $\bar{A}$, $\bar{\Phi}$, $\bar{A}_N$, and $\bar{\phi}_N$ corresponding to $\bar{c}(z)$. The quantities A and Φ represent the total-field amplitude and phase, respectively, and the integer N_{max} is the number of significant rays. Expressions for A_N and ϕ_N in Eq. (32) are given by Eqs. (20) and (10), respectively. The total-field

amplitude and phase are determined from

$$A^2 = [\sum_{N=1}^{N_{max}} A_N \sin(2\pi\phi_N)]^2 + [\sum_{N=1}^{N_{max}} A_N \cos(2\pi\phi_N)]^2, \quad (33a)$$

and

$$\sin(2\pi\Phi) = A^{-1} \sum_{N=1}^{N_{max}} A_N \sin(2\pi\phi_N), \cos(2\pi\Phi) = A^{-1} \sum_{N=1}^{N_{max}} A_N \cos(2\pi\phi_N), \quad (33b)$$

respectively, and similarly for $\bar{A}$ and $\bar{\Phi}$. If we define $\Delta A \equiv A - \bar{A}$, the total-field logarithmic amplitude anomaly (in dB) is

$$\Delta L \equiv 20\log_{10}(A/\bar{A}) = 20\log_{10}(1+\Delta A/\bar{A}). \quad (34a)$$

The total-field phase difference (in cycles) is

$$\Delta\Phi \equiv \Phi - \bar{\Phi}, \quad (34b)$$

and is represented here by values on the interval $[-\frac{1}{2}, \frac{1}{2}]$ cycles.

The total-field phase and amplitude differences depend only on per-ray phases and amplitudes, corresponding values of which for each N are close on $[R_L, R_{II}]$. However, this fact alone is not sufficient to guarantee that $\Delta\Phi$ and ΔL are small for all ranges in $[R_L, R_{II}]$, since small differences in individual quantities might conceivably combine so as to make $\Delta\Phi$ or ΔL not negligible. On the other hand, from our previous results we can expect that per-ray differences are particularly small on $[R_L, R_I]$ (and a substantial range subinterval of $(R_I, R_{II}]$). Therefore, for many c(z) profiles, positive total-field sensitivity results can be anticipated for a sizable portion of $[R_L, R_{II}]$.

To facilitate the determination of those ranges where total-field phase and amplitude differences are small, we seek to present simple approximations for $\Delta\Phi$ and ΔL. We define the dimensionless quantity ε_{MN} for $M \neq N$

as the phase-perturbation difference in radians between rays M and N,

$$\epsilon_{MN} \equiv 2\pi(\Delta\phi_M - \Delta\phi_N) \quad , \qquad 1 \leq M, N \leq N_{max}. \tag{35a}$$

We also define $\overline{\delta\Phi}_N$ as the difference in radians between the phase of ray N and the total-field phase using the $\bar{c}(z)$ profile:

$$\overline{\delta\Phi}_N \equiv 2\pi(\bar{\phi}_N - \bar{\Phi}) \quad , \qquad 1 \leq N \leq N_{max}. \tag{35b}$$

We note that in our subsequent development, $\overline{\delta\Phi}_N$ is not required to be small. Our approximations for $\Delta\Phi$ and ΔL involve a generalization of those presented for the cases $N_{max} = 2$ and 3 in Ref. 25, for which three assumptions are employed: (1) The ϵ_{MN} quantities are sufficiently small compared to one; (2) $\Delta A/\bar{A}$ is small enough so that the total-field equations may be expanded in this quantity; and (3) A_N can be approximated by $\bar{A}_N$ for all N. The first assumption is satisfied in our situation because we showed in Secs. II and III that on $[R_L, R_{II}]$ all per-ray phase differences are small and vary with range in a monotone fashion. The second assumption holds because we employ the approximations where $\Delta\Phi$ and ΔL are small and because from Eq. (34a) ΔL is small if and only if $\Delta A/\bar{A}$ is small. The third assumption is certainly true on $[R_L, R_I]$, where all per-ray amplitude differences are insignificant, as well as for some portions of the range interval $(R_I, R_{II}]$ where per-ray amplitude differences are relatively small. We improve the approximation to ΔL in Ref. 25 by not requiring (3), above, but rather that differences in per-ray amplitudes [or, equivalently, that ΔL_N in Eq. (25)] are small. A similar modification could be effected for the approximation to $\Delta\Phi$; however, from numerical calculations, this change improves the accuracy of the $\Delta\Phi$ approximation very little, so we omit this modification here.

Our approximations for any range in $[R_L, R_{II}]$ are

$$\Delta\Phi \doteq \Delta\phi_M - (2\pi)^{-1} \sum_{\substack{N=1 \\ N\neq M}}^{N_{max}} \varepsilon_{MN} (\bar{A}_N/\bar{A}) \cos(\overline{\delta\Phi}_N), \tag{36}$$

and

$$\Delta L \doteq d[\sum_{\substack{N=1 \\ N\neq M}}^{N_{max}} \varepsilon_{MN} (A_N/\bar{A}) \sin(\overline{\delta\Phi}_N) + H(R-R_I) \sum_{N=1}^{N_{max}} \eta_N (\bar{A}_N/\bar{A}) \cos(\overline{\delta\Phi}_N)]. \tag{37}$$

In Eqs. (36) and (37), M is any fixed integer between 1 and N_{max}, η_N is given by Eq. (24b), d is specified below Eq. (25), and H denotes the Heaviside function. We do not give the rather lengthy derivation of Eqs. (36) and (37) for arbitrary N_{max}, remarking only that the skew-symmetry of ε_{MN} (i.e., $\varepsilon_{MN} = -\varepsilon_{NM}$) enables any choice of M in these equations to yield the same values for $\Delta\Phi$ and ΔL. On $(R_I, R_{II}]$ the quantity $\Delta\phi_1$ appearing in Eqs. (36) and (37) is zero, while all other per-ray phase differences which appear there are represented on $[R_L, R_I]$ (or $(R_I, R_{II}]$) by the approximations of Eq. (16a) [or Eq. (30a)]. The use of approximate, rather than exact, per-ray phase difference formulas in our total-field phase- (and amplitude-) difference approximation is numerically fully satisfactory at most ranges in $[R_L, R_{II}]$ where $\Delta\Phi$ (and ΔL) is small. However, as R approaches R_I (or R_{II}) the critical $\Delta\phi_1$ (or $\Delta\phi_2$) approximation is typically an overestimate [see, for example, Fig. 2 (or Fig. 4) from 15-20 km (or 33-45.2 km)], which could cause Eqs. (36) and (37) to overestimate the sizes of the total-field phase and amplitude differences. We note that Eqs. (36) and (37) are valid under suitably weak assumptions which permit their application both to other sensitivity problems and also to situations where environmental or other variations produce small relative changes in phases and/or amplitudes of individual ray arrivals.

Before applying our approximations for $\Delta\phi$ and ΔL to determine ranges where total-field phase and amplitude using the profile $\bar{c}(z)$ are acceptably close to those for $c(z)$, we first discuss some features of them via an example. Using the hyperbolic-linear profile $c^{(H)}(z)$ of Fig. 1(a), its bilinear comparison profile $\bar{c}^{(H)}(z)$, and a source frequency of 200 Hz, we calculated exact (and approximate) values of $\Delta\phi$ and ΔL on $[R_L, R_{II}]$ = [1 km, 45.2 km] from Eqs. (34b) and (34a) [and Eqs. (36) and (37)], with $N_{max} = 4$. Both $\Delta\Phi$ and ΔL oscillate rapidly as range varies, so their values were computed with range increments of 0.01 km, with several additional calculations using 0.001 km increments to check the less refined results. Figure 6 (and 7) shows graphs of upper and lower bounds for $\Delta\Phi$ (and ΔL) associated with the $c^{(H)}(z)$ and $\bar{c}^{(H)}(z)$ profiles, for ranges from 1 km to 40 km. These exact (solid curves) and approximate (dashed curves) bounds are obtained by interpolating through the computed maximum and minimum values of $\Delta\Phi$ and ΔL on 1 km intervals. The discontinuities in the bounds occuring in both Figs. 6 and 7 at R_I = 20 km arise where $\bar{c}^{(H)}_I(z)$ is replaced by $\bar{c}^{(H)}_{II}(z)$. A schematic sample of the graph of $\Delta\Phi$ (and ΔL) itself is included in Fig. 6 (and 7) from 9-13 km (and 9-13 km and 26-30 km), although $\Delta\Phi$ (and ΔL) actually oscillates more rapidly than suggested in the schematic. We stress that despite these characteristic noise-like fluctuations, both $\Delta\Phi$ and ΔL typically assume values on any given range interval which are significantly greater than their lower bounds and smaller than their upper bounds.

We focus next on the $\Delta\Phi$ results in Fig. 6. The bounds show clearly that $\Delta\Phi$ is small for all ranges shown in Fig. 6. Moreover, we see that $\Delta\Phi$ is miniscule ($|\Delta\Phi| < 0.004$ cycles) from 20 km to about 32 km, the range interval where per-ray phase differences are smallest for this example (see Fig. 4). If the

$\Delta\phi_1$ curve in Fig. 2 were superimposed on Fig. 6 from 1 to 20 km, it would lie between the bounds in Fig. 6. This clear qualitative and quantitative similarity between $\Delta\phi_1$ and $\Delta\Phi$ indicates that at least for shorter ranges, $\Delta\Phi$ tends to be dominated by the first rays. Thus, taking $M = 1$ in Eq. (36) for ranges in $[R_L, R_I]$, we note that the first term on the right side of Eq. (36) is the more significant. The bound approximations are seen from Fig. 6 to be very good from 1 km to about 34 km, and to deteriorate somewhat beyond 34 km. We note that the overestimate of $|\Delta\Phi|$ by Eq. (36), mentioned previously, occurs in the dashed lower bound beyond 34 km. This overestimate of the approximate $\Delta\Phi$ bounds and the fact that $|\Delta\Phi|$ typically assumes values significantly less than these bounds should be taken into account when the acceptable tolerance Q_p for total-field phase differences is selected. Recalling our choice of q_p for the per-ray phase difference tolerance, we select $Q_p = 0.10$ cycles. We, therefore, conclude via Eq. (36) that the total-field phase using the profile $\bar{c}^{(H)}(z)$ acceptably approximates that using $c^{(H)}(z)$ on the entire interval $[R_L, R_{II}] = [1 \text{ km}, 45.2 \text{ km}]$.

Before discussing the total-field amplitude anomaly in Fig. 7, we give an example from another transmission problem which shows that propagation-loss differences can be large for profiles which possess very similar features. In one portion of a study[2] mentioned earlier, shallow-water propagation losses associated with eight decreasing profiles composed of linear segments are compared. All of these profiles possess the same surface and bottom sound speed and average gradient. Depth-averaged normal-mode propagation losses (incoherently summed) for these profiles were computed for a water depth of 100 m, ranges up to 100 km, and a source frequency of 200 Hz. Propagation-loss differences among these profiles amounted to as much as 3 dB at 20 km, 10 dB at 50 km, and 20 dB at 100 km. Returning to the total-field amplitude anomaly

for the $c^{(H)}(z)$ and $\bar{c}^{(H)}(z)$ profiles, we see that Fig. 7 shows small values of ΔL from 1 km to about 35 km. Very small values for $\Delta L(|\Delta L| < 0.25$ dB) occur over the same range interval, 20-32 km, and for the same reason that $\Delta\Phi$ has its smallest values. On the other hand, above about 33 km, values for $|\Delta L|$ become large fairly rapidly. The behavior of ΔL at these ranges can be attributed to the combined effects of increasing per-ray phase (principally $\Delta\phi_2$) as well as amplitude (principally ΔL_1) differences. In constrast, such volatile growth does not occur for ranges below R_I, because only per-ray phase differences significantly affect ΔL at these ranges. The occurrence of non-negligible per-ray amplitude differences on $(R_I, R_{II}]$, following their absence on $[R_I, R_{II}]$, suggests an explanation for the upward shift of the bounds curves on $(R_I, R_{II}]$, following their near-symmetry on $[R_L, R_I]$. In fact, the midpoints between the bounds in Fig. 7 are positive and increase with range on $(R_I, R_{II}]$, in a manner entirely consistent with the qualitative behavior of ΔL_1 in Fig. 5. We also note that the dashed curves in Fig. 7 are very good approximations to the exact bounds from 1 km to about 33 km and deteriorate beyond 33 km. As with the total-field phase difference, the overestimate of the approximations in Fig. 7 occurs here also. Taking into account the overestimates of the approximate ΔL formulas and the fact that $|\Delta L|$ assumes values that are typically much less than these bounds, we select a total-field amplitude tolerance Q_A of twice q_A or 0.8 dB. Then, we can conclude via Eq. (37) that the total-field amplitude using the profile $\bar{c}^{(H)}(z)$ acceptably approximates that of $c^{(H)}(z)$ for ranges on the interval [1 km, 33.3 km]. Combined with our discussion of total-field phase for this example, this conclusion extends to the entire received total field. Finally, we note that the range interval of acceptable total-field

correspondence in this example coincides largely with ranges where either per-ray phase or amplitude differences are insignificant, as might be expected.

V. SUMMARY

In this paper we present methods to replace a given sound-speed profile in certain transmission problems by a simpler profile so that corresponding acoustic quantities are negligibly different. The profiles considered here belong to a general class of depth-dependent, single-minimum profiles which model the deep-ocean sound channel. Using ray theory, we investigate surface reflecting/bottom reflecting transmissions between fixed source and receiver located on or near the ocean boundaries and separated by a short-to-medium range distance. We focus on procedures for constructing a simpler, comparison profile of bilinear type, but the principal features of our technique are sufficiently general to allow extensions to other types of comparison profiles.

For shorter ranges, the bilinear comparison profile is constructed by setting its depth-averaged sound speed equal to that of the specified profile. In addition, the SOFAR-axis depth and the surface and bottom sound speeds of the two profiles are matched. This method identifies the sound-speed data mean, along with profile data near certain ocean depths, as critical in determining the characteristics of received transmissions. Thus, when results of our analysis apply, key properties of the data, rather than the accurate matching of a sound-speed profile at all data points, are primary. The ray geometries associated with the specified and comparison profiles are shown to be very close. In particular, at each range under consideration, there is exactly the same number of received rays of each type associated with each

profile, and the surface and bottom angles and the Snell's law constants of corresponding rays are nearly identical. As a consequence of the method of constructing the comparison profile, the per-ray phases and amplitudes associated with the comparison profile approximate well those of the specified profile on some interval of shorter ranges. Relatively simple analytical approximations to the differences in per-ray phases and amplitudes between the two profiles are developed. Among other uses, these approximations lead to an easy way for determining precisely the aforementioned interval of shorter ranges, as a function of cw source frequency and of specified tolerances of acceptable phase and amplitude differences.

These conclusions, which can be referred to as positive per-ray sensitivity results, are then extended to longer ranges by means of a different procedure for construction of a bilinear comparison profile. The key element of the extension is to choose a bilinear profile so that the per-ray phase difference is negligible for the rays with the minimum number of boundary reflections. Other conditions for the determination of the comparison profile are the same as for the shorter-range case except that only the difference between the surface and bottom sound speeds is matched, rather than the values themselves. The longer-range bilinear comparison profile, which differs slightly depending on the source-receiver range, is found to be a small perturbation of the shorter-range comparison profile. Therefore, the ray geometries as well as the per-ray phases and amplitudes associated with a specified profile and its comparison profile remain very close. Useful per-ray phase and amplitude difference approximations are presented which specify the range interval where the per-ray quantities correspond closely. The overall length of the range interval is shown to be the same, provided the sound source and receiver are

located on the same ocean boundary. For a typical sound-channel profile consisting of linear and hyperbolic-cosine segments, this interval extends from 1 km to 45.2 km. If the source and receiver are located on opposite ocean boundaries, the interval of positive per-ray sensitivity results is more than half the length of that when the source and receiver are on the same boundary.

Comparisons of the received total field for a specified profile and its bilinear replacement profile are also performed. Simple approximate formulas are presented for total-field phase and amplitude differences between the two profiles; these formulas represent a major extension of previously known results. The approximations are general enough to be applicable both to other sensitivity problems and to studies where environmental or other variations produce small relative changes in acoustic quantities of individual ray arrivals. The approximation are exploited here to construct accurate upper and lower bounds for total-field differences. The bounds are shown to be small for ranges where per-ray results match closely. Further, they determine those ranges of acceptably good total-field correspondence, which for a typical example and for reasonable tolerance criteria are [1 km, 45.2 km] (and [1 km, 33.3 km]) for total-field phases (and amplitudes).

In future work the authors plan to extend the techniques and results of this initial investigation to study sound-speed profile replacement for other acoustic configurations. These may include varieties of given and comparison profiles, longer source-receiver ranges, source and receiver locations away from ocean boundaries, other types of ray transmissions, situations involving receiving arrays as well as point receivers, and different ocean boundary models. For such problems, we expect that well-approximating the ray geometry and per-ray acoustic quantities associated with the given profile would have an

important impact on the choice of both comparison profile type and its parameters. It is also anticipated that simple approximation to acoustic differences in individual ray quantities and in total-field variations would assist in formulating the construction procedure for the comparison profile and in specifying its range of utility.

1 L. P. Solomon and W. C. Merx, J. Acoust. Soc. Am. 56, 1126-1130 (1974).

2 P. H. Rogers, "Onboard prediction of propagation loss in shallow water," NRL Report 8500 (September 1981).

3 M. A. Pedersen, J. Acoust. Soc. Am. 33, 465-474 (1961).

4 M. A. Pedersen and D. F. Gordon, J. Acoust. Soc. Am. 41, 419-438 (1967).

5 M. A. Pedersen, J. Acoust. Soc. Am. 43, 619-634 (1968).

6 W. H. Munk, J. Acoust. Soc. Am. 55, 220-226 (1974).

7 J. C. Miller, J. Acoust. Soc. Am. 71, 859-862 (1982).

8 R. F. Henrick, M. J. Jacobson, and W. L. Siegmann, J. Acoust. Soc. Am 67, 121-134 (1980).

9 R. N. Baer and M. J. Jacobson, J. Acoust. Soc. Am. 57, 569-576 (1975).

10 R. N. Baer and M. J. Jacobson, J. Acoust. Soc. Am. 54, 80-91 (1973).

11 Summary Technical Report of DIV 6, NDRC, Vol. 8, 51-58 (1946).

12 N. L. Weinberg, J. G. Clark, and R. P. Flanagan, J. Acoust. Soc. Am. 56, 447-458 (1974).

13 I. M. Besieris and W. E. Kohler, SIAM J. Appl. Math. 34, 423-436 (1978).

14 D. White, J. Acoust. Soc. Am. 69, 436-442 (1981).

[15] C. E. Eckart, "A simple sound channel," MPL Tech. Memo. 211 (February 1970).

[16] C. B. Moler and L. P. Solomon, J. Acoust. Soc. Am. 48, 739-744 (1970).

[17] R. P. Flanagan, N. L. Weinberg, and J. G. Clark, J. Acoust. Soc. Am. 56, 1673-1680 (1974).

[18] C. B. Officer, Introduction to the Theory of Sound Transmission (McGraw-Hill, New York, 1958), p. 51.

[19] R. C. Buck, Advanced Calculus (McGraw-Hill, New York, 1978) p. 178.

[20] Ref. 18, pp. 74-83.

[21] K. G. Hamilton, W. L. Siegmann, and M. J. Jacobson, J. Acoust. Soc. Am. 67, 1193-1206 (1980).

[22] N. Jacobson, Basic Algebra I (W. H. Freeman and Co., San Francisco, 1974), pp. 257-258.

[23] J. T. Warfield and M. J. Jacobson, J. Acoust. Soc. Am. 50, 342-347 (1971).

[24] P. Henrici, Elements of Numerical Analysis (Wiley, New York, 1964), pp. 77-90.

[25] K. G. Hamilton, W. L. Siegmann, and M. J. Jacobson, J. Acoust. Soc. Am. 66, 1108-1119 (1979).

TABLE I. Numerical values for the parameters used in the $c^{(H)}(z)$ and $\bar{c}_I^{(H)}(z)$ profiles

Parameter	$c^{(H)}(z)$ profile	$c_I^{(H)}(z)$ profile
z_u (m)	527.16	
$z_a, \bar{z}_a$	1073.47	1073.47
z_ℓ	2194.33	
$z_b, \bar{z}_b$	4900.00	4900.00
$c_s, \bar{c}_s$ (ms^{-1})	1541.40	1541.40
c_u	1507.57	
$c_a, \bar{c}_a$	1490.08	1482.00
c_ℓ	1498.88	
$c_b, \bar{c}_b$	1541.40	1541.40
$c_\mu, \bar{c}_\mu$	1511.70	1511.70
$g_u, \bar{g}_u$ (s^{-1})	-0.0641738	-0.0553402
$g_\ell, \bar{g}_\ell$	0.0157171	0.0155247
k_u (m^{-1})	2.80226×10^{-4}	
k_ℓ	9.69122×10^{-5}	

FIGURE LEGENDS

Fig. 1. (a) Hyperbolic-linear sound-speed profile $c^{(H)}(z)$ and shorter range bilinear comparison profile $\bar{c}_I^{(H)}(z)$. (b) First half-lobes of corresponding rays.

Fig. 2. Exact (solid) and approximate (dashed) per-ray phase differences (cycles) vs. range (km) for N = 1 to 3 rays corresponding to $c^{(H)}(z)$ and $\bar{c}_I^{(H)}(z)$ profiles. Frequency f = 200 Hz.

Fig. 3. Exact (solid) and approximate (dashed) per-ray amplitude differences (dB) vs. range (km) for N = 1 and 2 rays corresponding to $c^{(H)}(z)$ and $\bar{c}_I^{(H)}(z)$ profiles.

Fig. 4. Exact (solid) and approximate (dashed) per-ray phase differences (cycles) vs. range (km) for N = 1 to 3 rays corresponding to $c^{(H)}(z)$ $\bar{c}_{II}^{(H)}(z)$ profiles. Frequency f = 200 Hz.

Fig. 5. Exact (solid) and approximate (dashed) per-ray amplitude differences (dB) vs. range (km) for N = 1 to 3 rays corresponding to $c^{(H)}(z)$ and $\bar{c}_{II}^{(H)}(z)$ profiles.

Fig. 6. Exact (solid) and approximate (dashed) bounds for total-field phase difference (cycles) vs. range (km) corresponding to $c^{(H)}(z)$ and $\bar{c}^{(H)}(z)$ profiles. Frequency f = 200 Hz.

Fig. 7. Exact (solid) and approximate (dashed) bounds for total-field amplitude difference (dB) vs. range (km) corresponding to $c^{(H)}(z)$ and $\bar{c}^{(H)}(z)$ profiles. Frequency f = 200 Hz.

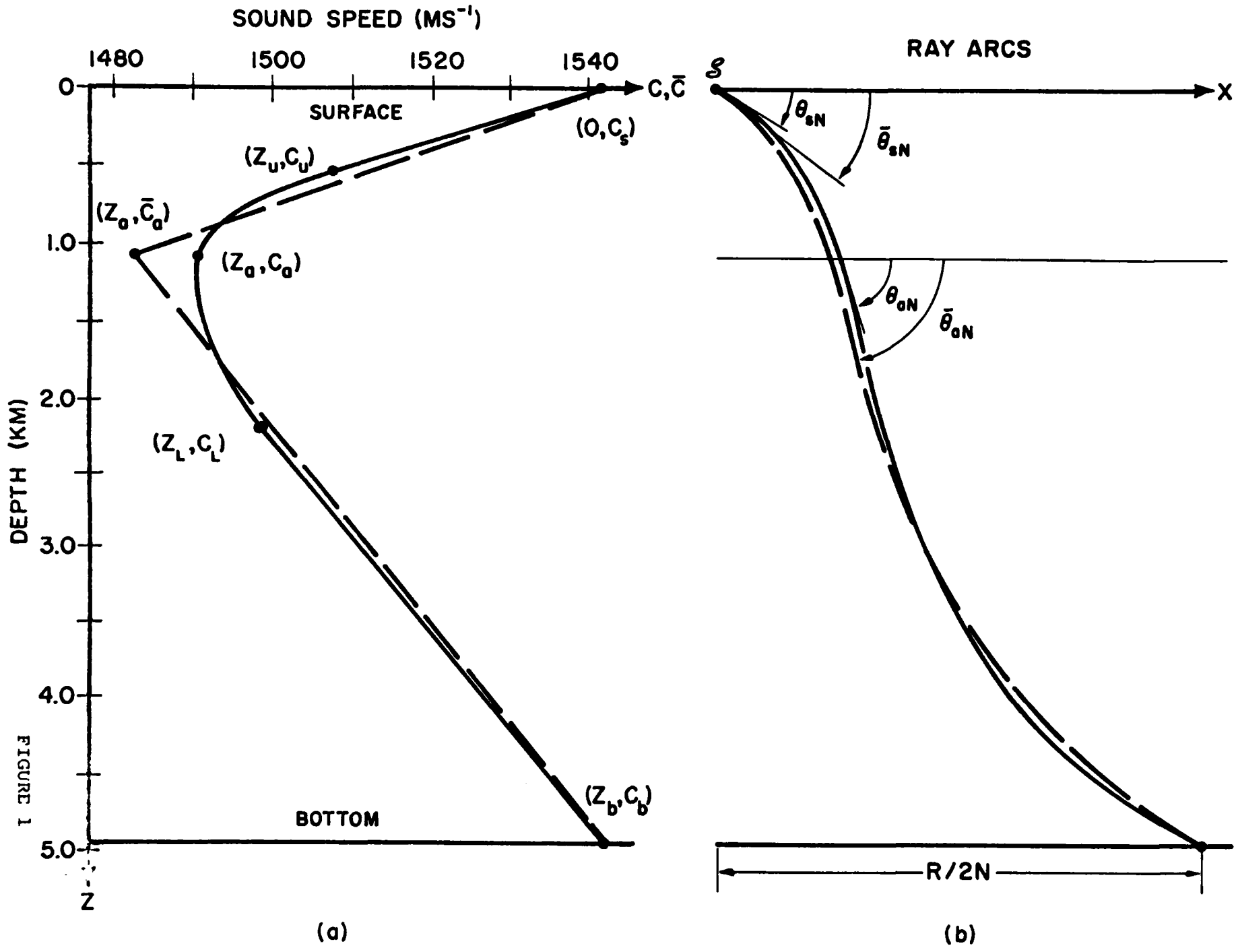
SOUND SPEED (MS⁻¹)
1480
1500
1520
1540
0
C, C̄
SURFACE
(0, C_s)
(Z_u, C_u)
(Z_a, C̄_a)
1.0
(Z_a, C_a)
(Z_L, C_L)
DEPTH (KM)
2.0
3.0
4.0
5.0
Z
(Z_b, C_b)
BOTTOM
(a)
RAY ARCS
S
X
θ_sN
θ̄_sN
θ_aN
θ̄_aN
R/2N
(b)

FIGURE 1

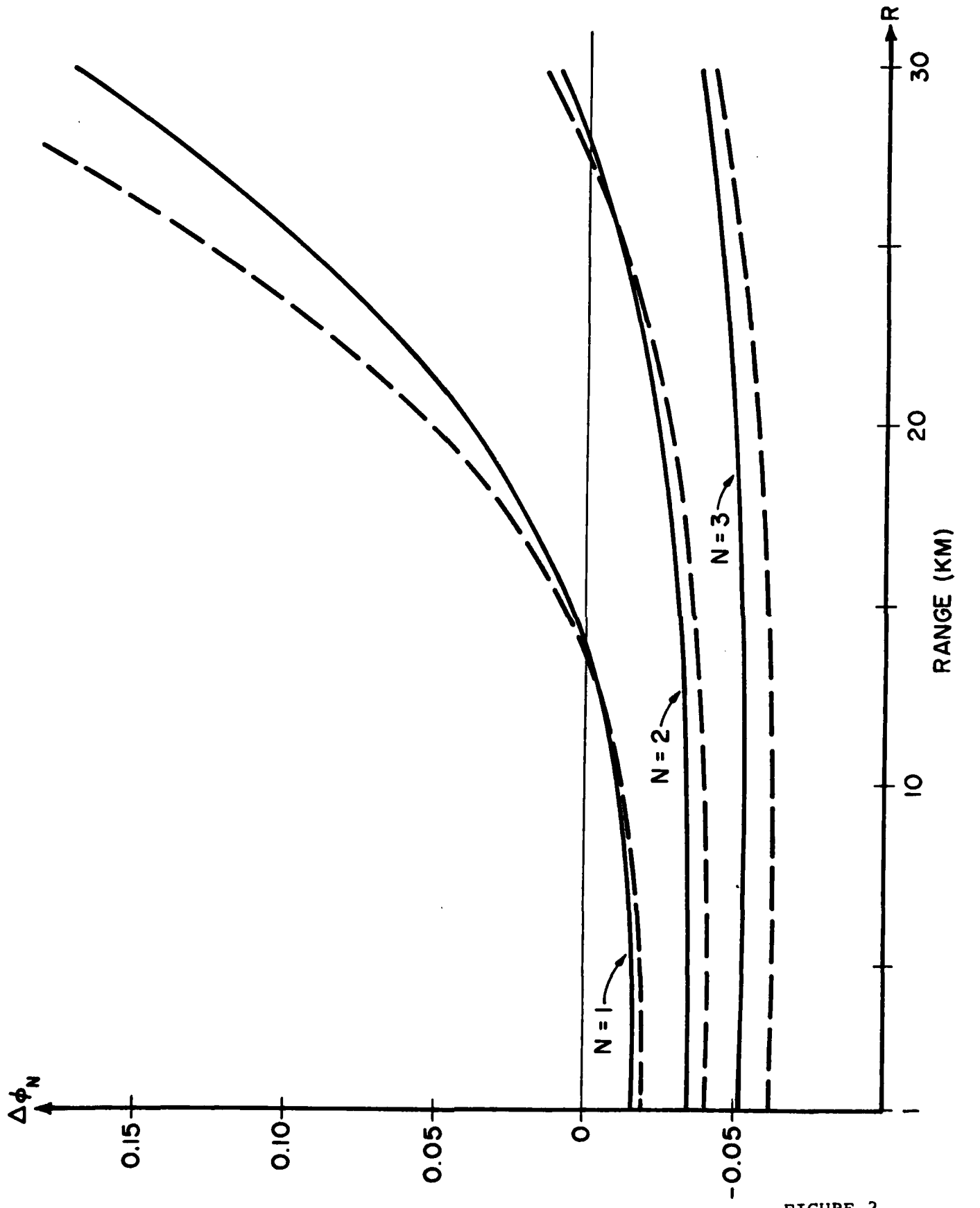
R
30
20
10
1
RANGE (KM)
N = 1
N = 2
N = 3
$\Delta\phi_N$
0.15
0.10
0.05
0
-0.05
PER-RAY PHASE DIFFERENCE (CYCLES)

FIGURE 2

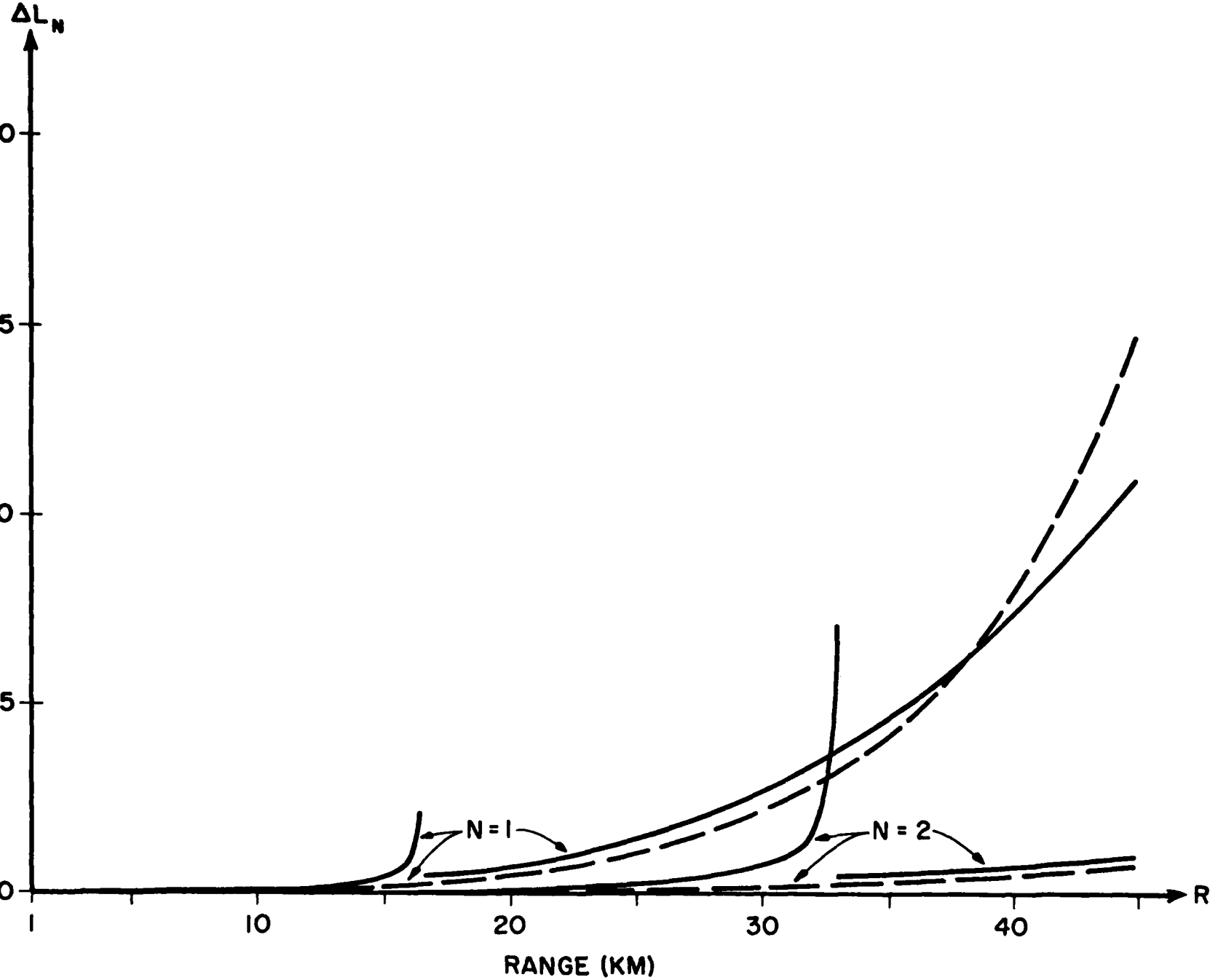
ΔL_N
0.20
0.15
0.10
0.05
0
PER-RAY AMP. DIFFERENCE (DB)
N = 1
N = 2
1
10
20
30
40
R
RANGE (KM)

FIGURE 3

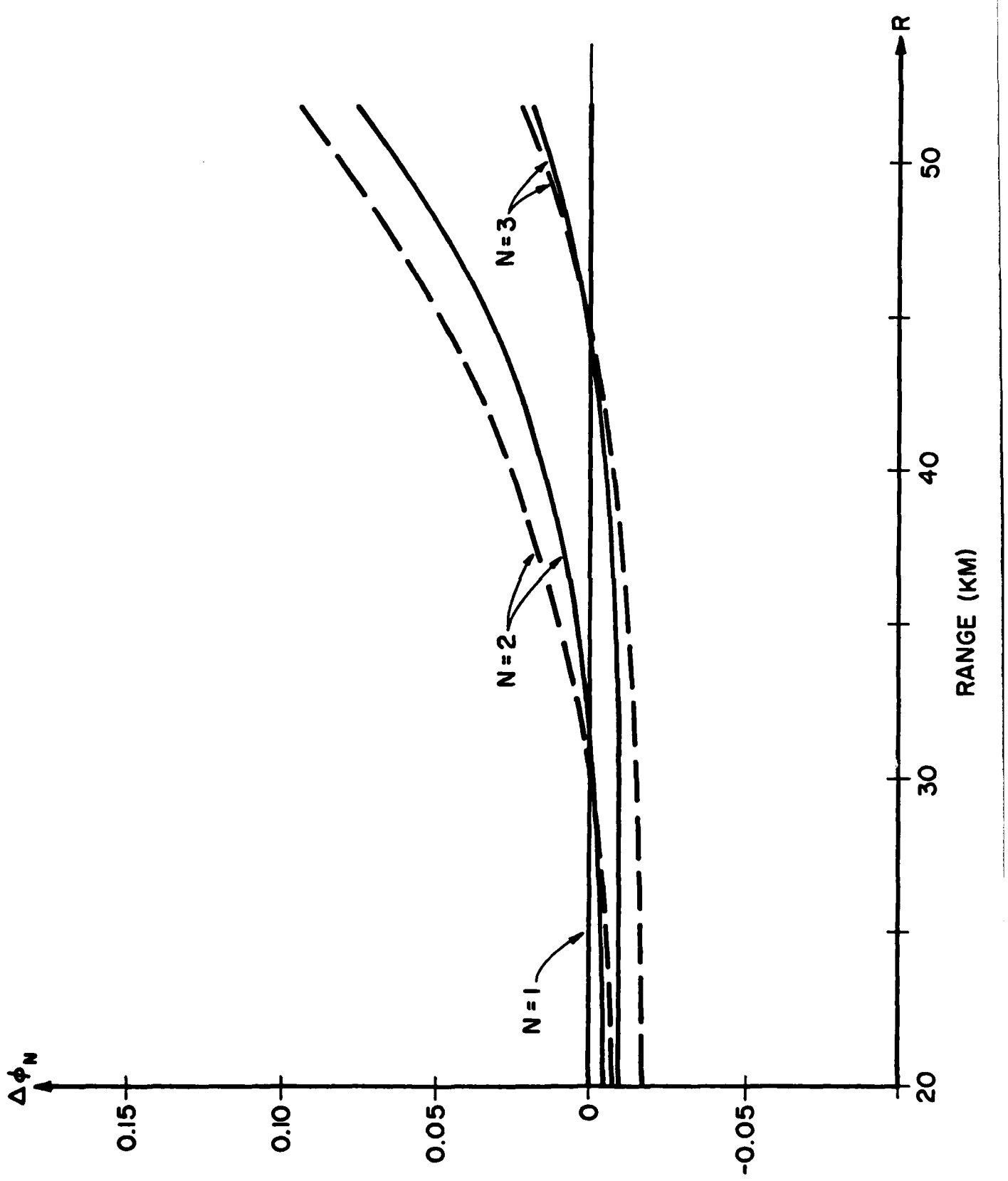
PER-RAY PHASE DIFFERENCE (CYCLES)
$\Delta\phi_N$
0.15
0.10
0.05
0
-0.05
N=1
N=2
N=3
R
20
30
40
50
RANGE (KM)

FIGURE 4

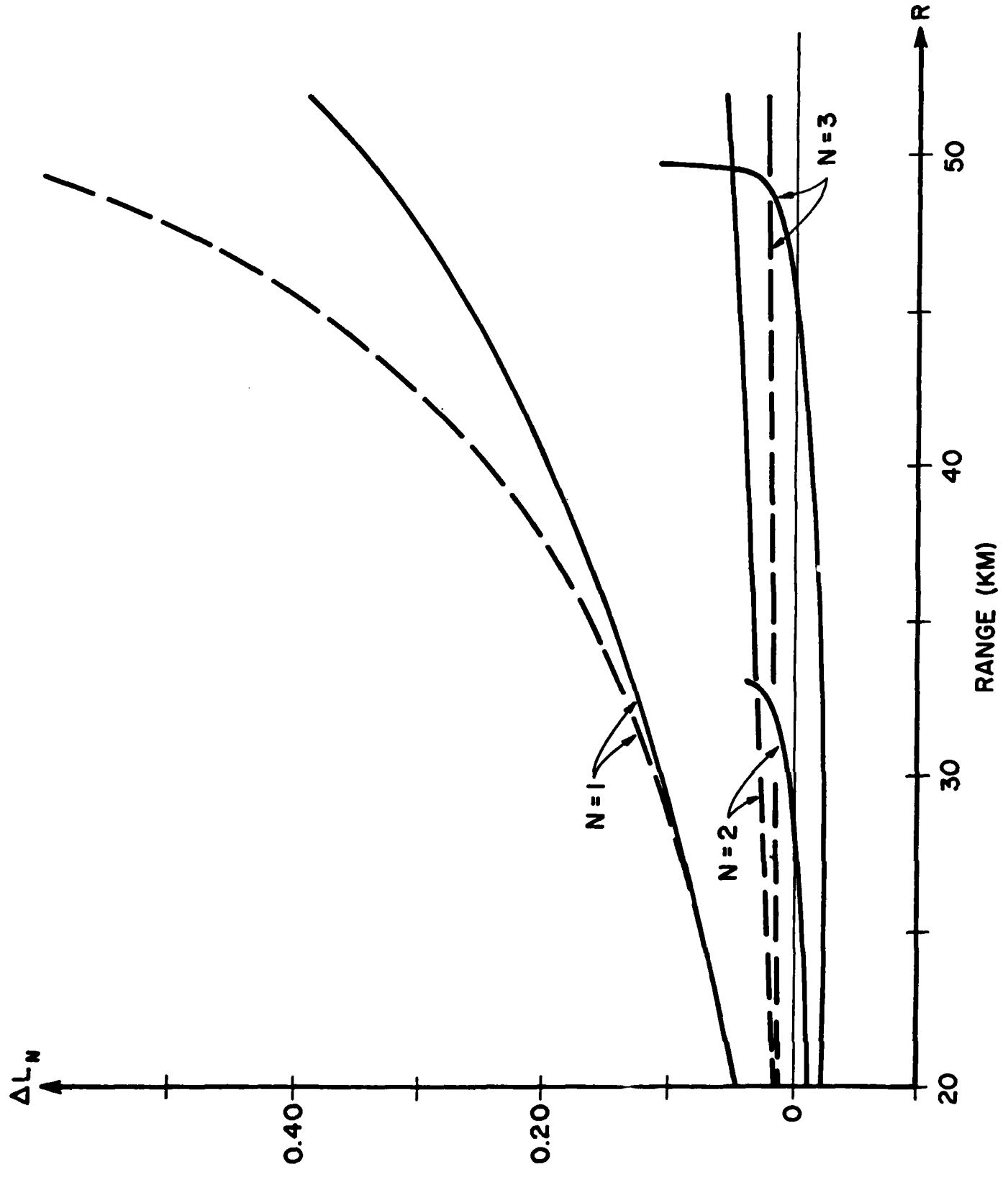
R
50
40
30
20
RANGE (KM)
N=3
N=2
N=1
ΔL_N
0.40
0.20
0
PER-RAY AMP. DIFFERENCE (DB)

FIGURE 5

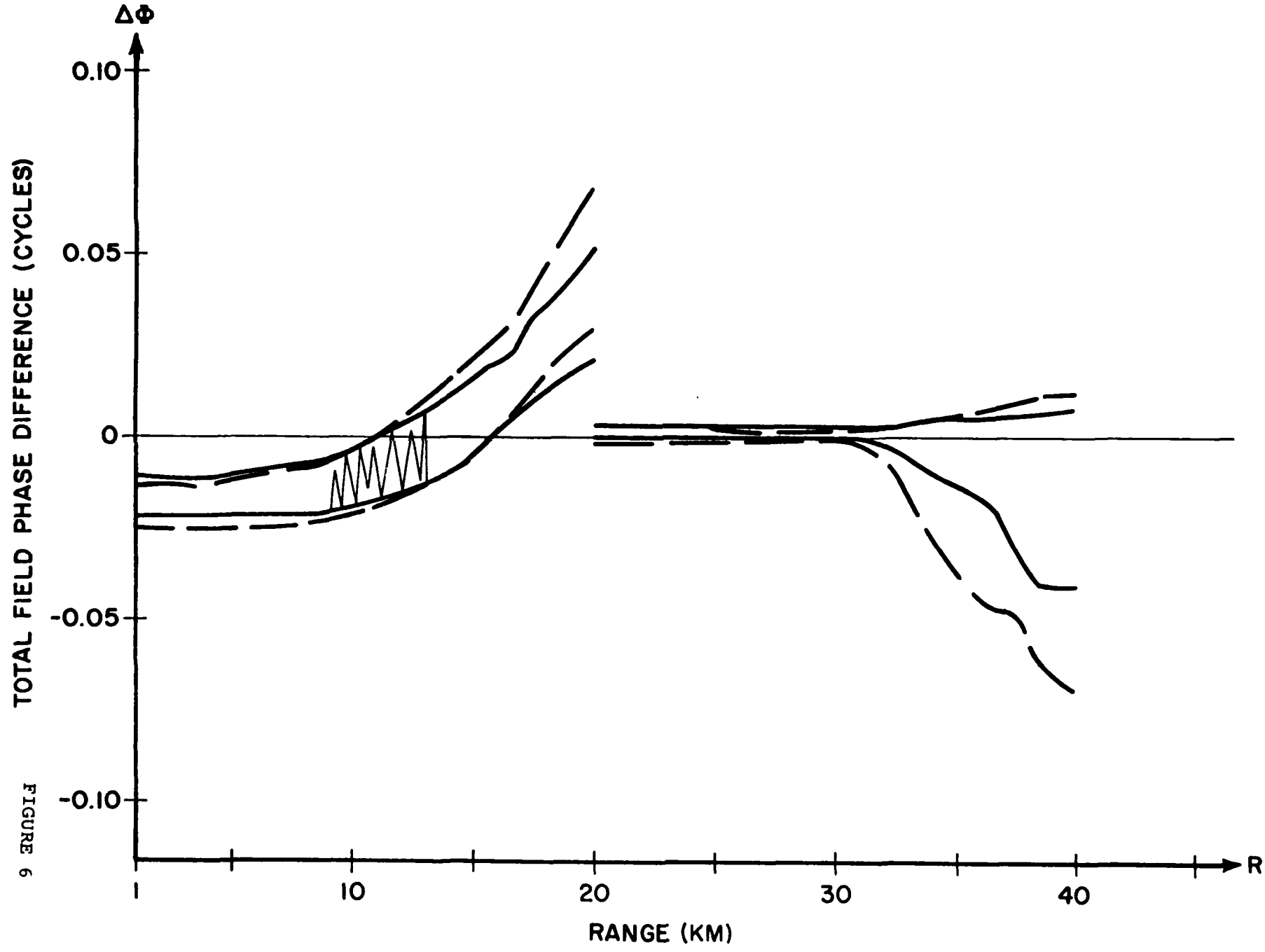
ΔΦ
0.10
0.05
0
-0.05
-0.10
TOTAL FIELD PHASE DIFFERENCE (CYCLES)
1
10
20
30
40
R
RANGE (KM)

FIGURE 6

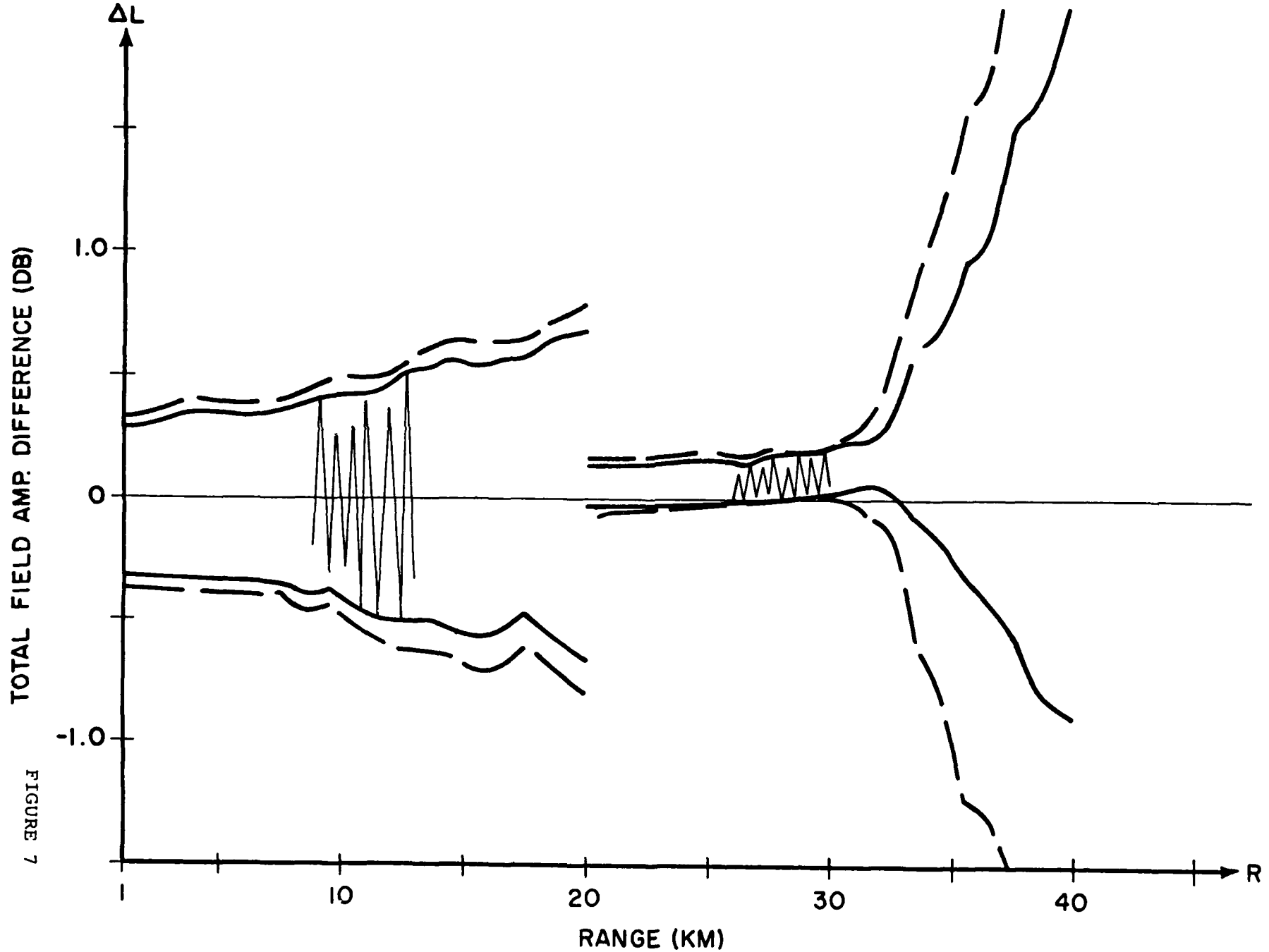

FIGURE 7

UNCLASSIFIED
DISTRIBUTION LIST
DEC 1981

Addressee	No. of Copies
Office of Naval Research 800 North Quincy Street Arlington, Virginia 22217	
Attn: Code 425AC	2
102	1
102C	1
210	1
220	1
Office of Naval Technology 800 North Quincy Street Arlington, Virginia 22217	
Attn: MAT 0721	1
MAT 0724	1
Director Naval Research Laboratory 4555 Overlook Avenue, SW. Washington, D.C. 20375	
Attn: Dr. J. C. Munson	1
Mr. R. R. Rojas	1
Dr. B. B. Adams	1
Dr. W. B. Moseley	1
Dr. J. P. Dugan	1
Unclassified Library	1
Superintendent Naval Research Laboratory Underwater Sound Reference Division P.O. Box 8337 Orlando, Florida 32806	1
Director Office of Naval Research Branch Office 1030 East Green Street Pasadena, California 91106	1
Office of Naval Research Rm 239, Campbell Hall University of California Berkeley, California 94720	1
Director Office of Naval Research Branch Office 495 Summer Street Boston, Massachusetts 02210	1
Office of Naval Research New York Area Office 715 Broadway - 5th Floor New York, New York 10003	1
Commanding Officer Office of Naval Research Branch Office Box 39 FPO New York 09510	1
Director Office of Naval Research Branch Office 536 South Clark Street Chicago, Illinois 60605	1
Office of Naval Research Resident Representative University District Building, Room 422 1107 North East 45th Street Seattle, Washington 98105	1

Addressee	No. of Cop
Technical Director Naval Oceanographic Research and Development Activity NSTL Station Bay St. Louis, Mississippi 39522	
Attn: Technical Director	1
Dr. L. Solomon	1
Dr. R. Gardner	1
Mr. E. Chaika	1
Mr. R. Van Wyckhouse	1
Dr. S. W. Marshall	1
Director Naval Oceanographic Office NSTL Station Bay St. Louis, Mississippi 39522	
Attn: Mr. H. Beck	1
Dr. T. M. Davis	1
Mr. W. H. Geddes	1
Dr. W. Jobst	1
Mr. R. Merrifield	1
Mr. R. A. Peloquin	1
Dr. M. K. Shank	1
Office of the Assistant Secretary of the Navy for Research, Engineering and Systems Washington, D.C. 20350	
Attn: Dr. D. Barbe, Rm 4E732 Pentagon	1
Dr. J. H. Probus, Rm 5E779 Pentagon	1
Chief of Naval Operations Room 5D580, Pentagon Washington, D.C. 20350	
Attn: OP951F	1
Commander Naval Sea Systems Command Department of Navy Washington, D.C. 20362	
Attn: Capt. James M. Van Metre PMS 409	1
Chief of Naval Operations Office of the Director Naval Oceanographic Division OP-952 Department of the Navy Washington, D.C. 20352	
Attn: Dr. R. W. James	1
Capt. J. C. Harlett	1
Commander Oceanographic System, Atlantic Box 100 Norfolk, Virginia 23511	1
Commander Oceanographic System, Pacific Box 1390 Pearl Harbor, Hawaii 96860	1

Addressee	No. of Copies
Defense Advanced Research Projects Agency 1400 Wilson Boulevard Arlington, Virginia 22209 Attn: Capt. V. Simmons	1
ARPA Research Center Moffett Field Unit #1 California 94035 Attn: Mr. E. Smith	1
Commanding Officer Fleet Weather Central Box 113 Pearl Harbor, Hawaii 96860	1
Naval Ocean Systems Center (Kaneohe) Kaneohe, Hawaii 96863 Attn: Mr. D. Hightower Mr. B. Kishimoto Mr. R. Buecher	1 1 1
Commander Naval Electronic Systems Command 2511 Jefferson Davis Highway National Center #1 Arlington, Virginia 20360 Attn: CAPT C. A. Rose,, PME 124 LCDR P. Girard, NAVELEX 612	2
Commander Naval Air Systems Command Jefferson Plaza #1 1411 Jefferson Davis Highway Arlington, Virginia 20360	1
Commander Naval Sea Systems Command National Center #2 2521 Jefferson Davis Highway Arlington, Virginia 20362 Attn: SEA 63R 63Y	1 1
Commanding Officer Fleet Numerical Weather Central Monterey, California 93940 Attn: Mr. Paul Stevens Dr. D.R. McLain (NMFS)	1 1
Defense Documentation Center Cameron Station Alexandria, Virginia 22314	12
Commander Naval Ocean Systems Center Department of the Navy San Diego, California 92132 Attn: Dr. Daniel Andrews Dr. Dean Hanna Mr. Henry Aurand Dr. Harry A. Schenck	1 1 1 1

Addressee	No. of Copies
Commander Naval Surface Weapons Center Acoustics Division Silver Spring, Maryland 20910	1
Commander Naval Surface Weapons Center Science and Mathematics Research Group (K05) Dahlgren, Virginia 22448 Attn: Dr. E.W. Schwiderski	1
Commanding Officer Naval Underwater Systems Center New London Laboratory New London, Connecticut 06320 Attn: Dr. William Von Winkle Dr. A. Nuttall Mr. A. Ellinthorpe Dr. D.M. Viccione Mr. A. Donn Cobb	1 1 1 1 1
Commander Naval Air Development Center Department of the Navy Warminster, Pennsylvania 18974 Attn: Unclassified Library	1
Commanding Officer Naval Coastal Systems Laboratory Panama City, Florida 32401 Attn: Unclassified Library	1
Commanding Officer Naval Underwater Systems Center Newport Laboratory Newport, Rhode Island 02840 Attn: Unclassified Library	1
Commander David W. Taylor Naval Ship Research and Development Center Bethesda, Maryland 20084 Attn: Dr. M. Sevik	1
Superintendent Naval Postgraduate School Monterey, California 93940	1
Superintendent U.S. Naval Academy Annapolis, Maryland 21402 Attn: Library	1
Commanding Officer Naval Intelligence Support Center 4301 Suitland Road Washington, D.C. 20390 Attn: NISC 20	1
Director Applied Physics Laboratory University of Washington 1013 North East 40th Street Seattle, Washington 98105 Attn: Dr. T.E. Ewart Dr. M. Schulkin	1 1

Addressee	No. of Copies
Applied Research Laboratories University of Texas at Austin P.O. Box 8029 10000 FM Road 1325 Austin, Texas 78712	
Attn: Dr. Loyd Hampton	1
Dr. Charles Wood	1
Atlantic Oceanographic and Meteorological Laboratories 15 Rickenbacker Causeway Miami, Florida 33149	
Attn: Dr. John Proni	1
Bell Telephone Laboratories 1 Whippany Road Whippany, New Jersey 07981	
Attn: Dr. Bruce Bogart	1
Dr. Peter Hirsch	1
Bolt, Beranek, and Newman, Inc. 50 Moulton Street Cambridge, Massachusetts 02238	
Attn: Dr. K. L. Chandiramani	1
Chase, Inc. 14 Pinckney Street Boston, Massachusetts 02114	
Attn: Dr. David Chase	1
Dr. David Middleton 127 East 91st Street New York, New York 10028	1
Duke University Department of Electrical Engineering Durham, North Carolina 27706	
Attn: Dr. Loren Nolte	1
General Electric Company Heavy Military Electronic Systems Syracuse, New York 13201	
Attn: Mr. Don Winfield	1
General Electric Company P.O. Box 1088 Schenectady, New York 12301	
Attn: Dr. Thomas G. Kincaid	1
Gould, Incorporated Chesapeake Instrument Division 6711 Baymeadow Drive Glen Burnie, Maryland 21061	
Attn: Dr. O. Lindemann	1
G R Associates, Inc. 10750 Columbia Pike Suite 602 Silver Spring, Maryland 20901	
Attn: Dr. Sheldon Gardner	
Dr. Frank Rees	
Hughes Aircraft Company P.O. Box 3310 Fullerton, California 92634	
Attn: Mr. S. W. Autrey	1

Addressee	No. of Copies
Hydroacoustics, Inc. 321 Northland Ave. P.O. Box 3818 Rochester, New York 14610	1
Institute for Acoustical Research Miami Division for the Palisades Geophysical Institute 615 South West 2nd Avenue Miami, Florida 33130	
Attn: Mr. M. Kronengold	1
Dr. J. Clark	1
Institute of Geophysics and Planetary Physics Scripps Institute of Oceanography University of California La Jolla, California 92093	
Attn: Dr. W. Munk	1
Mr. J. Spiesberger	1
Jaycor Incorporated 205 South Whiting Street Suite 607 Alexandria, Virginia 22304	
Attn: Dr. S. Adams	1
Massachusetts Institute of Technology Acoustics and Vibration Laboratory 70 Massachusetts Avenue Room 5-222 Cambridge, Massachusetts 02139	
Attn: Professor Patrick Leehey	1
Palisades Sofar Station Bermuda Division of Palisades Geophysical Institute FPO New York 09560	
Attn: Mr. Carl Hartdegen	1
Polar Research Laboratory 123 Santa Barbara Avenue Santa Barbara, California 93101	
Attn: Mr. Beaumont Buck	1
Research Triangle Institute Research Triangle Park Durham, North Carolina 27709	
Attn: Dr. S. Huffman	1
Rensselaer Polytechnic Institute Troy, New York 12181	
Attn: Dr. Melvin J. Jacobson	
Science Applications, Inc. 8400 Westpark Drive McLean, Virginia 22102	
Attn: Dr. P. Tatro	
S.D.P. Inc. 15250 Ventura Boulevard Suite 518 Sherman Oaks, California 91403	
Attn: Dr. M. A. Basin	1

Addressee	No. of Copies
Texas Instruments, Inc. 13500 North Central Expressway Dallas, Texas 75231 Attn: Mr. Charles Black	1
Underwater Systems, Inc. 8121 Georgia Avenue Silver Spring, Maryland 20910 Attn: Dr. M. Weinstein	1
University of Miami Rosenstiel School of Marine and Atmospheric Sciences 4600 Rickenbacker Causeway Miami, Florida 33149 Attn: Dr. H. DeFerrari	1
University of Michigan Department of Aerospace Engineering, North Campus Ann Arbor, Michigan 48109 Attn: Dr. W. W. Wilmarth	
University of Michigan Cooley Electronics Laboratory Ann Arbor, Michigan 48105 Attn: Dr. T. G. Birdsall	
University of Rhode Island Department of Electrical Engineering Wakefield, Rhode Island 02881 Attn: Dr. Donald Tufts	1
Woods Hole Oceanographic Institution Woods Hole, Massachusetts 02543 Attn: Dr. Paul McElroy Dr. R. Spindel	1 1

Unclassified

SECURITY CLASSIFICATION OF THIS PAGE (When Data Entered)

REPORT DOCUMENTATION PAGE		READ INSTRUCTIONS BEFORE COMPLETING FORM
1. REPORT NUMBER RPI Math. Rep. No. 136	2. GOVT ACCESSION NO.	3. RECIPIENT'S CATALOG NUMBER
4. TITLE (and Subtitle) Sensitivity to sound speed of surface/bottom reflecting transmissions in a deep ocean channel.		5. TYPE OF REPORT & PERIOD COVERED 6. PERFORMING ORG. REPORT NUMBER
7. AUTHOR(s) W. L. Siegmann, M. J. Jacobson, and P. B. Bilazarian		8. CONTRACT OR GRANT NUMBER(s) N00014-76-C-0288
9. PERFORMING ORGANIZATION NAME AND ADDRESS Rensselaer Polytechnic Institute Troy, New York 12181		10. PROGRAM ELEMENT, PROJECT, TASK AREA & WORK UNIT NUMBERS NR 386-606
11. CONTROLLING OFFICE NAME AND ADDRESS Office of Naval Research, Code 425 Department of the Navy Arlington, Virginia 22217		12. REPORT DATE 1 February 1983 13. NUMBER OF PAGES 57
14. MONITORING AGENCY NAME & ADDRESS(if different from Controlling Office)		15. SECURITY CLASS. (of this report) 15a. DECLASSIFICATION/DOWNGRADING SCHEDULE

16. DISTRIBUTION STATEMENT (of this Report)

This document has been approved for public release and sale; its distribution is unlimited.

17. DISTRIBUTION STATEMENT (of the abstract entered in Block 20, if different from Report)

18. SUPPLEMENTARY NOTES

19. KEY WORDS (Continue on reverse side if necessary and identify by block number)

Sound-Speed Profiles
Ray Theory
Total-Field Phase and Amplitude

20. ABSTRACT (Continue on reverse side if necessary and identify by block number)

The sensitivity of oceanic sound transmissions to the choice of a sound-speed profile is analyzed using ray theory. The profile may be selected from a large depth-dependent collection which models the deep ocean sound channel. Sound propagation is examined between fixed source and receiver, both close to

DD FORM 1 JAN 73 1473 EDITION OF 1 NOV 65 IS OBSOLETE
S/N 0102-LF-014-6601

Unclassified

SECURITY CLASSIFICATION OF THIS PAGE (When Data Entered)

horizontal ocean boundaries, for ranges up to about 50 km. Given a specified profile, procedures are prescribed for constructing a second, simpler profile so that important acoustic quantities are virtually identical. The construction methods are easy to apply, have physical interpretations, and identify the critical aspects of profile data which influence transmissions. The ray geometries associated with the two profiles are shown to be very close. Useful formulas are derived which demonstrate that per-ray and total-field phases and amplitudes corresponding to the simpler profile approximate accurately those of the specified profile. Schemes are presented for determining range intervals for replacement of the given profile, based on specified tolerances for phase and amplitude differences. Thus, when our procedure is applied, propagation results are not sensitive to the type of profile selected.